Two-dimensional numerical modelling of shallow water flows over multilayer movable beds

Thomas Rowan[1] Mohammed Seaid[2,*]

[1] *Department of Civil and Environmental Engineering, Imperial College London, SW7 2AZ, UK*
[2] *Department of Engineering, University of Durham, South Road, Durham DH1 3LE, UK*

Abstract

The two-dimensional modelling of shallow water flows over multi-sediment erodible beds is presented. A novel approach is developed for the treatment of multiple sediment types in morphodynamics. The governing equations include the two-dimensional shallow water equations for hydrodynamics, an Exner-type equation for morphodynamics, a two-dimensional transport equation for the suspended sediments, and a set of empirical equations for entrainment and deposition. Multilayer sedimentary beds are formed of different erodible soils with sediment properties and new exchange conditions between the bed layers are developed for the model. The coupled equations yield a hyperbolic system of balance laws with source terms. As a numerical solver for the system, we implement a fast finite volume characteristics method. The numerical fluxes are reconstructed using the method of characteristics which employs projection techniques. The proposed finite volume solver is simple to implement, satisfies the conservation property and can be used for two-dimensional sediment transport problems in non-homogeneous isotropic beds without need of complicated three-dimensional equations. To assess the performance of the proposed models, we present numerical results for a wide variety of shallow water flows over sedimentary layers. Comparisons to experimental data for dam-break problems over movable beds are also included in this study.

Keywords. Shallow water flows; Sediment transport; Multilayer beds; Suspended sediments; Finite volume method; Method of characteristics

1 Introduction

Modeling the phenomena of sediment transport in shallow water flows has become an active area of research in the past decades. In general, there are three techniques for modelling sediment transport namely, i) partial differential equations for which hydrodynamics and morphodynamics equations are used to predict the events, see for example [2, 25], ii) predictions made by analyzing and interpolating empirical data, either in equilibrium equations or with pure data analysis, see for instance [33, 17] and iii) hybrid models where elements of both techniques are utilized, see for example the ESTMORPH model [38]. For modelling morphodynamics in shallow water flows, the three most popular models are the Grass model [14], the Meyer-Peter & Muller model [22] and the Van-Rijn model [34]. Recently, a lot of work has been done for the simulation of sediment transport in rivers, for review we refer the reader to [36]. Modeling and numerical simulation of sediment transport in coastal regions have also been subject of research in [4, 18]. Modeling sediment transport using the well-established shallow water equations coupled with a conservation equation for the species concentration and a Exner-type equation for the bed-load have also been investigated in [25, 30, 20, 16] among others. Prior to these studies, a great deal of research was done to develop uncoupled

*Corresponding author: m.seaid@durham.ac.uk

models for which the hydrodynamics were solved first and then the effects on the bed were calculated. **However, coupled approaches are often more accurate for higher energy interactions where the timescale of morphological changes is similar to that of the flow such as those taken places in dam-break problems, see the discussions reported in [13] among others.**

The main limitation in the models studied in [25, 30, 20, 4] is the number of assumptions needed for their validation including the levels of armoring, vegetation, homogeneity, composition and compaction. These assumptions often lead to a large disconnect between experimental measurements and numerical simulations when compared with real-world applications. Recently many corrections have been proposed to improve these assumptions, see for example [11, 23]. However, the assumptions on the homogeneous and isotropic nature of the beds are the most severe limitations in these models, as naturally deposited soils are mixed and incorporate multiple soil types making them complex to model with an averaged sediment type only. **Accurate modelling of sediment sizes in order to reflect the constituents of both anthropogenic and natural landscapes has been carried out for instance in [1, 23], though this is not the most complex problem as natural layers are generally more homogeneous.** Man-made banks, flood and coastal defenses are often layered with fine graded soils deposited on top of each other (due to mechanical properties, permeability, fertility, cost, and other considerations). This leads to the complex case where several sediments have different erosion and deposition rates creating intricate profiles for morphological changes. **Although the most modern models are able to deal with complex water flows, the area of complex sediments remains relatively unresolved, compare [20, 18, 5, 15] for a diverse set of approaches. In the present study we propose a new coupled model for two-dimensional shallow water flows over multilayer erodible beds. Notice that other models accounting for multiple sediments were studied in [15] but these models yield complex eigenvalues in their formulation. The current work deals with multiple sediments only in the erosion and deposition terms and keep a register of sediment fractions enabling the use of averages to avoid complex eigenvalues in the system.** We assume that the bed is heterogeneous and constituted with multiple layers of different sediment properties. The structure of soil-superposed packed beds and the total number of layers to be considered in the analysis are fixed a priori. To the best of our knowledge, simulation of two-dimensional shallow water flows over multilayer erodible beds **including superposed heterogeneous beds** is presented for the first time.

In the current work, the bed is reformulated as a function of three-dimensional variables and its discretization is carried out using control volumes. A fill factor is assigned for each control volume, which can be either fully filled by a single-sediment type or partially filled of multiple sediments of different types. The top filled control volume is then treated as the bed floor and surpassed when it is overfilled or totally eroded. At the same time, a margin of empty control volumes are incorporated above the initial active volume to allow for morphological variation. Sediment types and their concentrations are set in suspension by storing individual concentrations for each control volume. Modeling multiple sediment types would normally require reformulating the conventional models of sediment transport to include more equations for conservation of species. In our study, introducing cumulative functions for the sediment concentration, sediment density, porosity and other sediment variables mitigates this complication. The resulting system consists only of five equations for conservation of mass, momentum, species and bed-load. For the entrainment and erosion we consider the empirical equations reported in [8, 26] with modifications to allow for discretized beds. To improve the accuracy in erosion and deposition terms, each sediment is evaluated separately when considering bed-load flux, and the proportions of sedimentary flux in the shallow water system are back calculated. The procedure leads to an accurate and consistent model for both hydrodynamics and morphodynamics. Furthermore, the proposed model allows for several further functions to be incorporated into the system, including tracking the origin and transport of particular types of sediments in the water flow. This is particularly useful for dam-break problems involving dangerous or contaminated sediments such as tailings dam failure investigated in [24].

Numerical solutions of the sediment transport models often present difficulties due to a combination of their nonlinear form, the presence of the source terms, and the coupling between the bed-load equation and the equations governing the water flow, **see for example [2, 21, 41].** Here, the main difficulty in the proposed model comes from the coupling terms involving derivatives of the unknown physical variables for the bed profile and sediment concentration. Because of the presence of these terms in the governing equations, a numerical method originally designed for solving shallow water flows over movable single-layer beds will lead to instabilities when it is applied to each bed layer separately. In the current work, we implement the Finite Volume of Characteristics (FVC) method developed for two-dimensional shallow water equations in [3]. The FVC method avoids the solution of Riemann problems and it can be viewed as a predictor-corrector finite volume method. The predictor step employs the method of characteristics to reconstruct the numerical fluxes whilst, the corrector step recovers the conservation equations in the finite volume framework. The results presented in [3] confirm that the FVC method is simple, conservative, non-oscillatory and suitable for shallow water equations over erodible beds for which Riemann problems are **computationally expensive to solve because of the complex nature of the eigenvalues involved in their mathematical formulation**. Several numerical examples are presented to verify the ability of the proposed model to accurately solve the two-dimensional shallow water flows over multilayer sedimentary beds. We first compare our simulations to experimental data for a test example of dam-break flows over single-layer erodible beds. Next we simulate similar flow problems over erodible multilayer beds and examine the performance of the proposed techniques using different numbers of layers in the sedimentary topography. Numerical results presented in this study demonstrate high resolution of the FVC method and confirm its capability to provide accurate and efficient simulations for sediment transport by water flows, including erosion and deposition effects in heterogeneous beds.

The rest of the paper is organized as follows: In Section 2, we introduce the two-dimensional governing equations for shallow water flows over multilayer movable sedimentary beds. Modeling mass-exchange terms between multilayer beds is described in Section 3. In Section 4, we formulate the finite volume of characteristics method for the numerical solution of developed system. Numerical results and examples are presented in Section 5. We examine the performance of the proposed model for several examples of shallow water flows over multilayer movable beds, and the comparison to experiments is also presented in this section. Conclusions are summarized in Section 6.

2 Modeling shallow water flows over multilayer movable beds

In general, the governing equations of shallow water flows over movable beds are derived by balancing the net inflow of mass, momentum, and species through the boundaries of a control volume whilst accounting for shallow water assumptions, see for example [7]. In a conservative form, these equations read

$$
\begin{aligned}
\frac{\partial H}{\partial t} + \frac{\partial (Hu)}{\partial x} + \frac{\partial (Hv)}{\partial y} &= \frac{E-D}{1-p}, \\
\frac{\partial (Hu)}{\partial t} + \frac{\partial}{\partial x}\left(Hu^2 + \frac{1}{2}gH^2\right) + \frac{\partial}{\partial y}(Huv) &= -gH\frac{\partial B}{\partial x} - \frac{(\rho_s-\rho_w)gH^2}{2\rho}\frac{\partial c}{\partial x} + \mathcal{S}_x, \\
\frac{\partial (Hv)}{\partial t} + \frac{\partial}{\partial x}(Huv) + \frac{\partial}{\partial y}\left(Hv^2 + \frac{1}{2}gH^2\right) &= -gH\frac{\partial B}{\partial y} - \frac{(\rho_s-\rho_w)gH^2}{2\rho}\frac{\partial c}{\partial y} + \mathcal{S}_y, \\
\frac{\partial (Hc)}{\partial t} + \frac{\partial (Hcu)}{\partial x} + \frac{\partial (Hcv)}{\partial y} &= E-D, \\
\frac{\partial B}{\partial t} &= \frac{D-E}{1-p},
\end{aligned}
\tag{1}
$$

where $H(t,x,y)$ is the water depth, $u(t,x,y)$ the averaged water velocity in the x-direction, $v(t,x,y)$ the averaged water velocity in the y-direction, $B(t,x,y)$ the bottom topography, $c(t,x,y)$ the averaged concentration of the suspended sediment, g the gravitational acceleration, p the porosity, ρ_w the water density, and ρ_s the sediment density. Here, E and D represent the total entrainment and deposition terms in upward

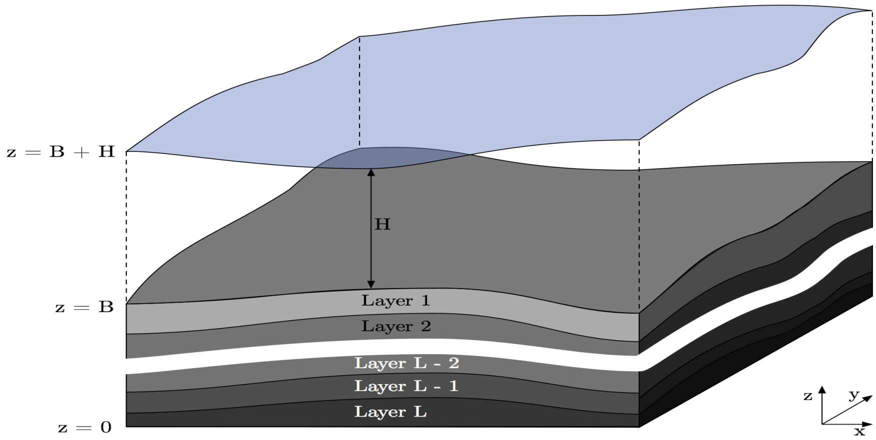

Figure 1: Sketch of a two-dimensional system of shallow-water flows over a multilayer bed.

and downward directions, respectively. In (1), the source term $\mathcal{S}_x$ and $\mathcal{S}_y$ are accounting for friction slopes and sediment reaction as

$$\mathcal{S}_x = -g\frac{n_b^2 u\sqrt{u^2+v^2}}{H^{1/3}} - \frac{(\rho_0-\rho)(E-D)u}{\rho(1-p)}, \qquad \mathcal{S}_y = -gH\frac{n_b^2 v\sqrt{u^2+v^2}}{H^{1/3}} - \frac{(\rho_0-\rho)(E-D)v}{\rho(1-p)},$$

where n_b is the Manning roughness coefficient, $\rho(t,x,y)$ the density of the water-sediment mixture, and ρ_0 the density of the saturated bed related to the sediment concentration and porosity by

$$\rho = \rho_w(1-c) + \rho_s c, \qquad \rho_0 = \rho_w p + \rho_s(1-p). \tag{2}$$

Note that the above relations are designed for the single layer bed and have to be modified for the multilayer sediment model as discussed below. In this case, the involved sediment parameters including the Manning roughness coefficient would vary from one layer to another in the bed. It should also be stressed that the above equations have been widely used in the literature to model sediment transport by shallow water flows, see for instance [2, 20] and further references therein. It is easy to verify that the system (1) is hyperbolic with five real and distinct eigenvalues given by [2]

$$\begin{aligned} &\lambda_1 = 0, \qquad \lambda_2 = u, \qquad \lambda_3 = u, \qquad \lambda_4 = u - \sqrt{gH}, \qquad \lambda_5 = u + \sqrt{gH},\\ &\mu_1 = 0, \qquad \mu_2 = v, \qquad \mu_3 = v, \qquad \mu_4 = v - \sqrt{gH}, \qquad \mu_5 = v + \sqrt{gH}. \end{aligned} \tag{3}$$

It should be mentioned that, the finite volume method proposed in this study does not require the calculation of the eigenvalues for the system but the estimation of the eigenvalues in (3) may be used for controlling the timestep size in the numerical simulations. Note that the equations (1) assume that the suspended sediments and the bed-load are isotropic and homogeneous formed with a single layer of soils. However, for many applications in realistic sediment transport, the topography is formed with multiple soils and often superposed in a set of layers. In the present work, we are interested in situations of shallow water flows over multilayer beds, as illustrated in Figure 1. Thus, the bed topography B in equations (1) depends also on the vertical direction z *i.e.*, $B = B(t,x,z)$. Here, we consider a system with multiple species of sediments ($m = 1,2,\ldots,M$) that can exist in a number of bed layers ($l = 1,2,\ldots,L$), with M and L are the total numbers of sediment species and the total number of layers in the bed, respectively. Notice that two or more layers may contain the same sediment species and a layer may also contain multiple sediment species.

In order to extend the equations (1) to sediment transport with multilayer beds, we introduce the cumulative sediment concentration

$$\overline{c} = \sum_{m=1}^{M} c_m,$$

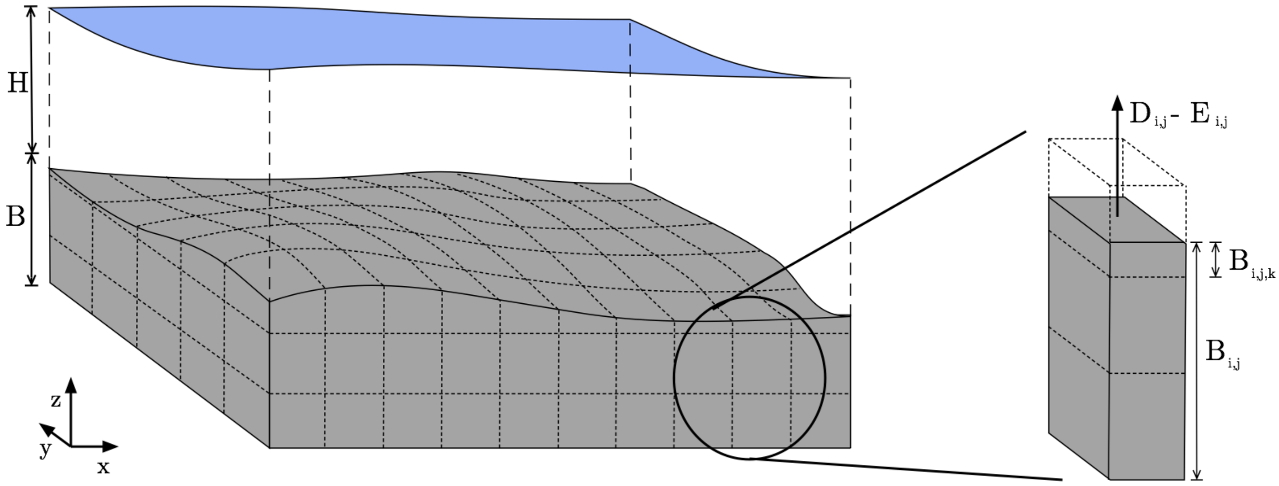

Figure 2: Vertical discretization of a single-layer bed with three mixed sediments into control volumes.

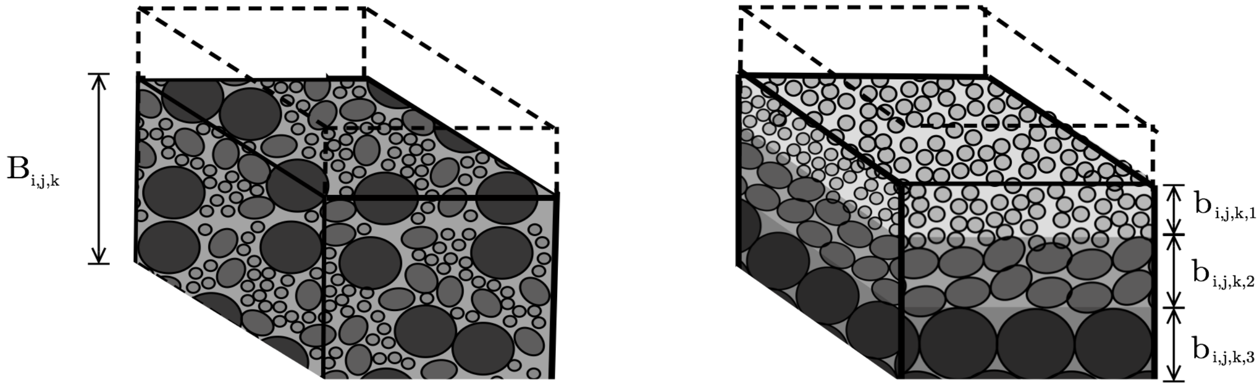

Figure 3: Reorganization of the mixed sediment species into discretized control volumes.

and we define the averaged sediment variables

$$\overline{\rho}_s = \sum_{m=1}^{M} \frac{c_m}{\overline{c}} \rho_{s,m}, \qquad \overline{\rho} = \rho_w (1 - \overline{c}) + \sum_{m=1}^{M} \frac{c_m}{\overline{c}} \rho_{s,m}, \qquad \overline{D} = \sum_{m=1}^{M} \frac{c_m}{\overline{c}} D_m. \tag{4}$$

Note that these sediment fractions are held in a register and updated at each time step in order to stop them being homogenized over successive time steps. Furthermore, the equivalent averaging procedure (4) does not increase the number of equations in the system (1), but it still allows for erosion and deposition to be handled separately for each type of sediment. Therefore, the proposed system efficiently models the different erosion and deposition characteristics of each sediment type, while not incurring significant additional computational cost.

For the remaining sediment variables $\overline{\rho}_0$, $\overline{E}$ and $\overline{p}$, we use the similar equivalent averaging but with respect to the sediment bed, instead of the suspended sediment. **To this end, we discretize the vertical z-direction into a set of control volumes $\left[B_{k-1/2}, B_{k+1/2}\right]$, $k = 1, 2, \ldots, K$ with K is the total number of control volumes. For simplicity only, we assume that these control volumes have**

a uniform size Δz, see Figure 2 for an illustration of a single-layer bed with three mixed sediments. Each control volume may contain different sediment species which need to be reorganized in a rigorous manner to be compatible with the governing equations. This allows us to contemplate the individual sediment mix in each control volume. **In order to perform this method, a register of bed volume fractions for each bed and flow control volume is hold during the time integration process. This enables us to handle the sediment as an average in both the flow calculations and individuals for interactions between the bed and the flow.**

The crucial assumption we make is that the height of the control volume is small enough that all sediment species in the control volume are able to interact with the water simultaneously and can be eroded or deposited. In Figure 3 we illustrate the method adopted in this study to reorganize sediment species in the bed topography. Here, the active top control volume has a height B_k, formed of three sediments with effective height in the cell of $b_{k,1}$, $b_{k,2}$ and $b_{k,3}$, respectively. Hence, the bed-dependent variables are calculated using the weighted averaging procedure [32] as

$$\overline{n}_b = \sum_{m=1}^{M} \frac{b_{k,m}}{B_k} n_{b,m}, \quad \overline{p} = \sum_{m=1}^{M} \frac{b_{k,m}}{B_k} p_m, \quad \overline{\rho}_0 = \rho_w(1-\overline{p}) + \sum_{m=1}^{M} \frac{b_{k,m}}{B_k} \rho_k, \quad \overline{E} = \sum_{m=1}^{M} \frac{b_{k,m}}{B_k} E_m.$$

Note that each control volume interacts only with its neighboring control volumes, whereas erosion and deposition only occur in the active top control volume. In the current study, to account for vertical exchanges in the bed we consider an Exner-type equation which ensures the sediment transfer between bed control volumes. Hence, the equations we consider for modelling shallow water flows over multilayer beds are

$$\begin{aligned}
\frac{\partial H}{\partial t} + \frac{\partial (Hu)}{\partial x} + \frac{\partial (Hv)}{\partial y} &= \frac{\overline{E} - \overline{D}}{1-\overline{p}},\\
\frac{\partial (Hu)}{\partial t} + \frac{\partial}{\partial x}\left(Hu^2 + \frac{1}{2} g H^2\right) + \frac{\partial}{\partial y}(Huv) &= -gH\frac{\partial B}{\partial x} - \xi g H^2 \frac{\partial \overline{c}}{\partial x} + \overline{\mathcal{S}}_x,\\
\frac{\partial (Hv)}{\partial t} + \frac{\partial}{\partial x}(Huv) + \frac{\partial}{\partial y}\left(Hv^2 + \frac{1}{2} g H^2\right) &= -gH\frac{\partial B}{\partial y} - \xi g H^2 \frac{\partial \overline{c}}{\partial y} + \overline{\mathcal{S}}_y,\\
\frac{\partial (H\overline{c})}{\partial t} + \frac{\partial (H\overline{c}u)}{\partial x} + \frac{\partial (H\overline{c}v)}{\partial y} &= \overline{E} - \overline{D},\\
\frac{\partial B}{\partial t} + \frac{\partial \mathcal{G}(B)}{\partial z} &= \frac{\overline{D} - \overline{E}}{1-\overline{p}},
\end{aligned} \tag{5}$$

where $\mathcal{G}(B)$ is a flux function which depends on the exchange terms between the bed control volumes and it is formulated below in section 3. **Note that, as in the models reported in [2, 20], the proposed model does not use horizontal bed fluxes in its formulation and all sediment interactions are represented in the erosion and deposition relations.** In (5),

$$\xi = \frac{(\overline{\rho_s} - \overline{\rho_w})}{2\overline{\rho}}, \quad \mathcal{S}_x = -g\frac{\overline{n}_b^2 u\sqrt{u^2+v^2}}{H^{1/3}} - \frac{(\overline{\rho_0} - \overline{\rho})(\overline{E} - \overline{D})u}{\overline{\rho}(1-\overline{p})}, \quad \mathcal{S}_y = -gH\frac{\overline{n}_b^2 v\sqrt{u^2+v^2}}{H^{1/3}} - \frac{(\overline{\rho_0} - \overline{\rho})(\overline{E} - \overline{D})v}{\overline{\rho}(1-\overline{p})}.$$

To determine the entrainment and deposition terms in the above equations we use empirical relations reported in [8] among others. Thus,

$$D_m = w_m \left(1 - C_{a,m}\right)^2 C_{a,m}, \tag{6}$$

where w_m is the deposition coefficient experimentally measured in [35, 39, 27], $C_{a,m} = \alpha_{c,m} c_m$ is the near-bed volumetric sediment concentration and $\alpha_{c,m}$ is a coefficient larger than unity to ensure that the near-bed concentration does not exceed $(1 - p_m)$. Here, the coefficient $\alpha_{c,m}$ is defined by [10]

$$\alpha_{c,m} = \min\left(2, \frac{1-p_m}{c_m}\right).$$

For the entrainment of sediments, the following empirical relation is used

$$E_m = \begin{cases} \varphi_m \dfrac{\theta_m - \theta_{c,m}}{H} \sqrt{u^2+v^2} d_m^{-0.2}, & \text{if} \quad \theta_m \geq \theta_{c,m}, \\ 0, & \text{otherwise}, \end{cases}$$

where φ_m is a coefficient to control the erosion forces, $\theta_{c,m}$ is a critical value of the Shields parameter for the initiation of sediment motion and θ is the Shields coefficient defined by

$$\theta_m = \frac{v_{*,m}^2}{s_m g d_m}, \tag{7}$$

where s_m is the submerged specific gravity of sediment given by

$$s_m = \frac{\rho_{s,m}}{\rho_w} - 1,$$

and $v_{*,m}$ is the friction velocity defined using the Darcy-Weisbach friction law as

$$v_{*,m}^2 = \sqrt{\frac{g\ n_{b,m}^2}{H^{1/3}}} \sqrt{u^2+v^2}.$$

Note that most formulae for models of suspended sediments, obtained from experiments and measured data, are empirical to differing extents, see for example [8, 9, 28]. Other empirical formulae for the erosion and deposition terms can also be used in the system (5) without major conceptual modifications. The equations (5) can also be rewritten in a compact vector form as

$$\frac{\partial \mathbf{W}}{\partial t} + \frac{\partial \mathbf{F}(\mathbf{W})}{\partial x} + \frac{\partial \mathbf{G}(\mathbf{W})}{\partial y} = \mathbf{Q}(\mathbf{W}) + \mathbf{R}(\mathbf{W}), \tag{8}$$

where

$$\mathbf{W} = \begin{pmatrix} H \\ Hu \\ Hv \\ H\overline{c} \\ B \end{pmatrix}, \qquad \mathbf{F}(\mathbf{W}) = \begin{pmatrix} Hu \\ Hu^2 + \frac{1}{2}gH^2 \\ Huv \\ Hu\overline{c} \\ 0 \end{pmatrix}, \qquad \mathbf{G}(\mathbf{W}) = \begin{pmatrix} Hv \\ Huv \\ Hv^2 + \frac{1}{2}gH^2 \\ Hv\overline{c} \\ 0 \end{pmatrix},$$

$$\mathbf{Q}(\mathbf{W}) = \begin{pmatrix} 0 \\ -gH\dfrac{\partial B}{\partial x} - \xi g H^2 \dfrac{\partial \overline{c}}{\partial x} \\ -gH\dfrac{\partial B}{\partial y} - \xi g H^2 \dfrac{\partial \overline{c}}{\partial y} \\ 0 \\ 0 \end{pmatrix}, \qquad \mathbf{R}(\mathbf{W}) = \begin{pmatrix} \dfrac{\overline{E} - \overline{D}}{1 - \overline{p}} \\ -\mathcal{S}_x \\ -\mathcal{S}_y \\ \overline{E} - \overline{D} \\ -\dfrac{\partial \mathcal{G}(B)}{\partial z} - \dfrac{\overline{E} - \overline{D}}{1 - \overline{p}} \end{pmatrix}.$$

It should be pointed out that since the flux function $\mathcal{G}(B)$ added in the bed-load is only differentiated with respect to z, the hyperbolic parts in the system (5) have not changed from those appearing in its conventional counterpart (1). Therefore, the eigenvalues associated with the system (8) are also given by the expressions (3).

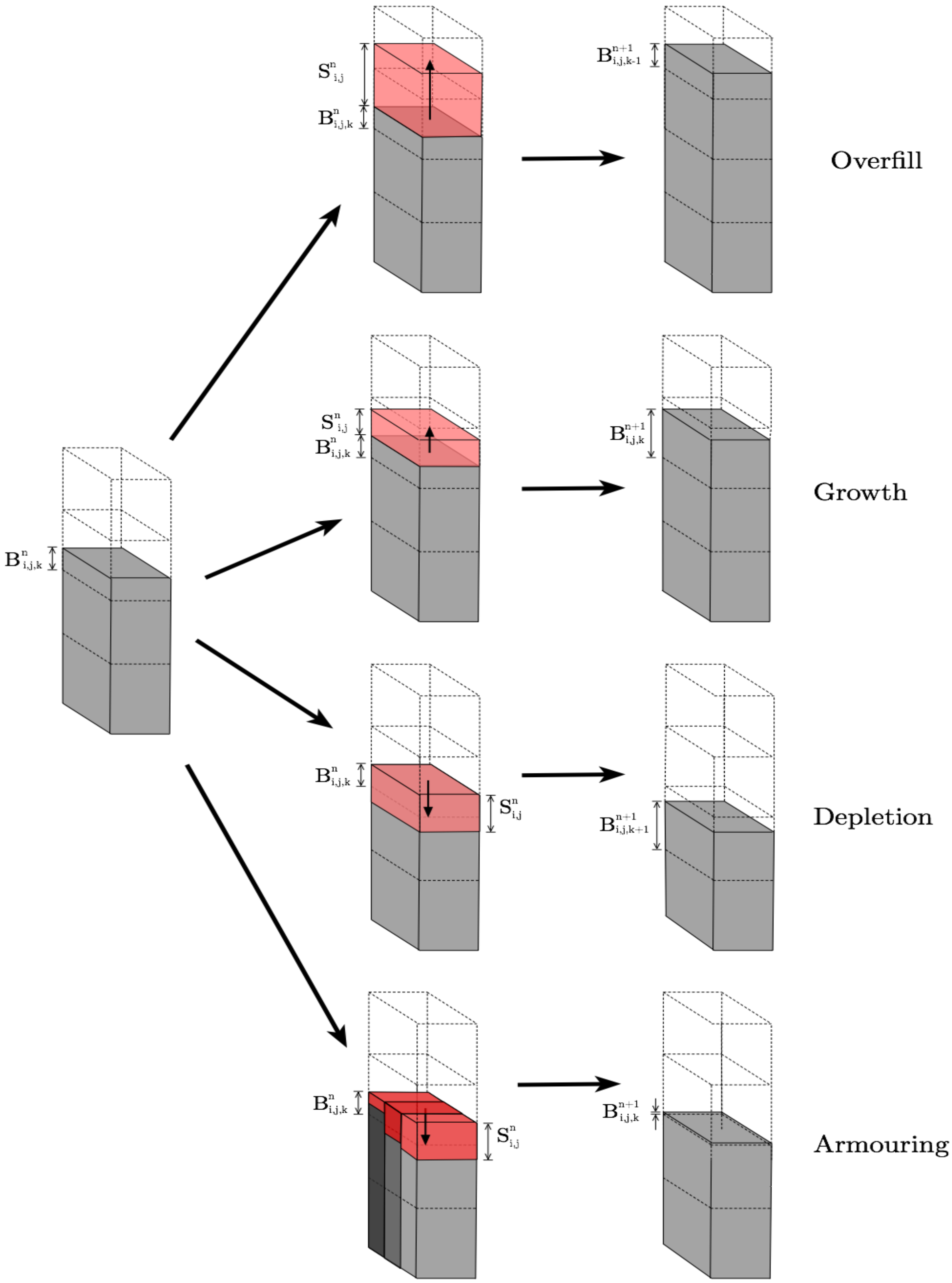

Figure 4: Illustration of different alterations in the control volumes for shallow water flows over multilayer beds considered in the current study.

3 Formulation of exchange terms for multilayer beds

To formulate the exchange terms $\mathcal{G}(B)$ for multilayer beds in (5) we consider the control volumes $[z_{k+1/2}, z_{k-1/2}]$ shown in Figure 3 and we divide the time interval into subintervals $[t_n, t_{n+1}]$ with uniform size Δt. Here, $t_n = n\Delta t$, $z_{k+1/2} = k\Delta z$ and $z_k = (k-1/2)\Delta z$ is the center of the control volume. Following the standard finite volume formulation, we integrate the bed-load equation in (5) with respect to time and space over the domain $[t_n, t_{n+1}] \times [z_{k+1/2}, z_{k-1/2}]$ to obtain the following discrete equation

$$B_k^{n+1} = B_k^n + \frac{\Delta t}{\Delta z}\left(\mathcal{G}_{k+1/2}^n - \mathcal{G}_{k-1/2}^n\right) + \Delta t \mathcal{P}_k^n, \tag{9}$$

where B_k^n is the depth-averaged bed B in the control volume $[z_{k+1/2}, z_{k-1/2}]$ at time t_n defined by

$$B_k^n(x,y) = \frac{1}{\Delta z}\int_{z_{k+1/2}}^{z_{k-1/2}} B(t_n, x, y, z)\, dz,$$

and $\mathcal{G}_{k\mp1/2}^n = \mathcal{G}(B_{k\mp1/2}^n)$ are the numerical fluxes at $z = z_{k\mp1/2}$ and time t_n. Since the erosion and deposition takes place only in the top active control volume, the source term in (9) is given by

$$\mathcal{P}_k^n = \begin{cases} -\dfrac{\overline{E}_k^n - \overline{D}_k^n}{1-\overline{p}_k} & \text{if} \quad z_{k+1/2} < B \le z_{k-1/2}, \\ 0, & \text{elsewhere.} \end{cases}$$

As with sediment fractions, the kth active (exposed) cell is stored in a register during the simulation and k is modified following the steps described in the algorithms below. This ensures that the correct cell value for k is eroded, maintained or surpassed depending on the case under study. Note that as $0 \le B_k^n \le \Delta z$, only four possible cases may occur for movable beds, as illustrated in Figure 4. These cases are:

i) Volume growth: Erosion and deposition rates in the control volume do not exceed the cell bounds.

ii) Volume depletion: The control volume is entirely eroded and the control volume below becomes active.

ii) Volume overfill: The control volume is overfilled and the control volume above becomes the active cell.

iv) Volume armoring: The control volume holds out against total erosion.

To formulate the flux functions $G_{k\mp1/2}^n$ in (9), we apply boundary conditions for the three first cases of homogeneous sediments. For instance, in the case of volume overfill, $B_k^{n+1} = \Delta z$ and $\mathcal{G}_{k+1/2}^n = 0$. Thus

$$\Delta z = B_k^n + \frac{\Delta t}{\Delta z}\left(-\mathcal{G}_{k-1/2}^n\right) + \Delta t \mathcal{P}_k^n,$$

which can be rearranged as

$$\mathcal{G}_{k-1/2}^n = \frac{\Delta z}{\Delta t}\left(B_k^n - \Delta z - \Delta t \frac{\overline{E}_k^n - \overline{D}_k^n}{1-\overline{p}_k}\right). \tag{10}$$

For the case of volume depletion, $B_k^{n+1} = 0$ and $\mathcal{G}_{k-1/2}^n = 0$. Thus

$$0 = B_k^n + \frac{\Delta t}{\Delta z}\left(\mathcal{G}_{k+1/2}^n\right) + \Delta t\ S_k^n,$$

Algorithm 1: Reconstruction of the bed in the homogeneous multilayer models.

if $B_{*,k}^{n+1} > \Delta z$ **then**

$B_k^{n+1} = \Delta z$

$B_{k-1}^{n+1} = B_k^n - \Delta z - \Delta t \dfrac{E_k^n - D_k^n}{1 - p_k}$

$k \longleftarrow k+1$

else if $B_{*,k}^{n+1} \leq 0$ **then**

$B_k^{n+1} = 0$

$B_{k+1}^{n+1} = B_k^n + \Delta z - \Delta t \dfrac{E_k^n - D_k^n}{1 - p_k}$

$k \longleftarrow k-1$

else

$B_k^{n+1} = B_{*,k}^{n+1}$

end

which can be rearranged as

$$\mathcal{G}_{k-1/2}^n = \frac{\Delta z}{\Delta t}\left(-B_{k-1}^n + \Delta t \frac{\overline{E}_{k-1}^n - \overline{D}_{k-1}^n}{1 - \overline{p}_{k-1}}\right). \tag{11}$$

For the case of volume growth, both upper and lower fluxes vanish and

$$\mathcal{G}_{k-1/2}^n = \begin{cases} \dfrac{\Delta z}{\Delta t}\left(B_k^n - \Delta z - \Delta t \dfrac{\overline{E}_k^n - \overline{D}_k^n}{1 - \overline{p}_k}\right), & \text{if} \quad B_k^n - \Delta t \dfrac{\overline{E}_k^n - \overline{D}_k^n}{1 - p_k} > \Delta z, \\ \dfrac{\Delta z}{\Delta t}\left(-B_{k-1}^n + \Delta t \dfrac{\overline{E}_{k-1}^n - \overline{D}_{k-1}^n}{1 - \overline{p}_{k-1}}\right), & \text{if} \quad B_k^n - \Delta t \dfrac{\overline{E}_{k-1}^n - \overline{D}_{k-1}^n}{1 - \overline{p}_{k-1}} < 0, \\ 0 & \text{otherwise.} \end{cases} \tag{12}$$

Note that the reconstruction of the flux functions $G_{k\mp1/2}^n$ requires only the evaluation of bed height in the three neighboring control volumes and it can be implemented for homogeneous beds using the test bed height

$$B_{*,k}^{n+1} = B_k^n + \Delta t \frac{\overline{E}_k^n - \overline{D}_k^n}{1 - \overline{p}_k}.$$

Hence, given the bed topography B_k^n at time t_n, the new bed topography B_k^{n+1} at time t_{n+1} is updated using Algorithm 1.

For the volume armoring, the sediment mixes between the bed and the flow and, to handle this, we assume that the volume height can be expressed as the sum of the heights of the sediments inside it as shown in Figure 3. For this case, we calculate the bed height $b_{*,k,m}$ at each time step as

$$b_{*,k,m}^{n+1} = b_{k,m}^n + \Delta b_{k,m}^n = b_{k,m}^n + \Delta t \left(\frac{E_{k,m}^n - D_{k,m}^n}{1 - p_{k,m}}\right),$$

where $b_{k,m}$ $(m = 1, 2, \ldots, M)$ are the corresponding heights of sediment contained within the control volume. We also define $\Delta b_{*,k}^-$ and $\Delta b_{*,k}^+$ as the sum of all negative and all positive $\Delta b_{j,k}$ sediment height changes in the control volume, respectively. Hence, the procedure to update the bed B_j^{n+1} for this case is described in Algorithm 2.

It should be stressed that for the case of volume armoring, inappropriate discretization of the bed may have a direct effect on the bed-load and suspended sediments. Thus, a lower limit on the vertical

Algorithm 2: Reconstruction of the bed in the non-homogeneous multilayer models.

if $\sum_{m=1}^{M} b_{*,k,m}^{n+1} \geq \Delta z$ **then**
  for $m = 1 : M$ **do**
    if $b_{*,k,m} \geq 0$ **then**
      $b_{k,m}^{n+1} = b_{k,m}^{n} + (\Delta z - B_k^n - \Delta b_{*,k}^{-}) \dfrac{\Delta b_{*k,m}^{n}}{\Delta b_{*,k}^{+} - \Delta b_{*,k}^{-}}$
      $b_{k-1,m}^{n+1} = \Delta b_{*,k,m}^{n+1} - (\Delta z - B_k^n - \Delta b_{*,k}^{-}) \dfrac{\Delta b_{*,k,m}^{n}}{\Delta b_{*,k}^{+} - \Delta b_{*,k}^{-}}$
    else
      $b_{k,m}^{n+1} = b_{*,k,m}^{n+1}$
    end
  end
  $k \longleftarrow k + 1$
else if any $m \in \{1, \ldots, M\}$ $b_{*,k,m}^{n+1} \geq 0$ **and** $\sum_{m=1}^{M} b_{*,k,m}^{n+1} \leq 0$ **then**
  for $m = 1 : M$ **do**
    if $b_{*,k,m} > 0$ **then**
      $b_{k,m}^{n+1} = b_{*,k,m}^{n+1}$
    else
      $b_{k,m}^{n+1} = 0$
      $\Delta b_{*,k,m}^{n} = -b_{k,m}^{n}$
    end
  end
else if all $b_{*,k,m}^{n+1} \leq 0$ **then**
  for $m = 1 : M$ **do**
    if $b_{*,k+1,m}^{n+1} > 0$ **then**
      $b_{k+1,m}^{n+1} = b_{k,m}^{n} + b_{k+1,m}^{n} - \Delta b_{*,k,m}^{n}$
    else
      $\Delta b_{*,k,m}^{n} = -b_{k,m}^{n}$
    end
    $b_{k,m}^{n+1} = 0$
  end
  $k \longleftarrow k - 1$
else
  for $m = 1 : M$ **do**
    $b_{k,m}^{n+1} = b_{*,k,m}^{n+1}$
  end
end

discretization is set using the largest particle size d. **This is a crucial parameter of the proposed model which requires tuning and fitting in the same manner as the spacial discretization of the flow in x and y directions. Therefore, for the multilayer discretization for which the armoring is possible, Δz should satisfy the following condition [16]**

$$\Delta z \geq 10d. \tag{13}$$

Note that, whilst the composition of the layers in the bed topography should be known in advance, the number of discretized layers in the algorithm can be set by the user, and two or more discretized layers may be formed with the same soil. **In practice, this would require appropriate judgment and possibly tuning to balance the overall efficiency and accuracy in the model.**

4 Numerical solution of shallow water flows over multilayer movable beds

APM-D-19-03367 In practice, the numerical solution of the equations (8) can be carried out using any finite volume method designed for solving hyperbolic systems of conservation laws with source terms. In the present study, we consider the Finite Volume Method of Characteristics (FVC) method studied in [3] for solving the shallow water equations over fixed beds. The main advantage of the FVC method over other finite volume methods lies in the absence of Riemann solvers in its reconstruction of numerical fluxes. The FVC method is also conservative, well balanced, second-order accurate, fast and simple to implement. In this section, we briefly describe the FVC formulation for solving the equations (8) and further details can be found in [3]. For the time integration of the system (8), we use the notation $\mathbf{W}^n$ to denote the value of a generic function $\mathbf{W}$ at time t_n. We also use the splitting operator introduced in [31] to deal with the differential source terms $\mathbf{Q}(\mathbf{W})$ and the non-differential source term $\mathbf{R}(\mathbf{W})$ in (8). The splitting procedure consists of the following two steps:

Step 1: Solve for $\mathbf{W}^*$

$$\frac{\mathbf{W}^* - \mathbf{W}^n}{\Delta t} = \mathbf{R}(\mathbf{W}^n). \tag{14}$$

Step 2: Solve for $\mathbf{W}^{n+1}$

$$\frac{\mathbf{W}^{n+1} - \mathbf{W}^*}{\Delta t} + \frac{\partial \mathbf{F}(\mathbf{W}^*)}{\partial x} + \frac{\partial \mathbf{G}(\mathbf{W}^*)}{\partial y} = \mathbf{Q}(\mathbf{W}^*). \tag{15}$$

For the space discretization of the equation (15) we consider control volumes $V_{i,j} = [x_{i-\frac{1}{2}}, x_{i+\frac{1}{2}}]\times[y_{j-\frac{1}{2}}, y_{j+\frac{1}{2}}]$ as shown in Figure 4. Each control volume $V_{i,j}$ is centered at (x_i, y_j) with uniform sizes Δx and Δy for simplicity in the presentation only. We also use the notations $\mathbf{W}^n_{i\pm\frac{1}{2},j} = \mathbf{W}(t_n, x_{i\pm\frac{1}{2}}, y_j)$, $\mathbf{W}^n_{i,j\pm\frac{1}{2}} = \mathbf{W}(t_n, x_i, y_{j\pm\frac{1}{2}})$, and

$$\mathbf{W}^n_{i,j} = \frac{1}{\Delta x}\frac{1}{\Delta y}\int_{x_{i-\frac{1}{2}}}^{x_{i+\frac{1}{2}}}\int_{y_{j-\frac{1}{2}}}^{y_{i+\frac{1}{2}}} \mathbf{W}(t_n, x, y)dydx,$$

to denote the point-values and the approximate cell-average of the variable $\mathbf{W}$ at the gridpoint $(t_n, x_{i\pm\frac{1}{2}}, y_j)$, $(t_n, x_i, y_{j\pm\frac{1}{2}})$, and (t_n, x_i, y_j), respectively. Hence, integrating the equation (15) with respect to space over the control volume $V_{i,j}$, one obtains the following discrete equations

$$\frac{\mathbf{W}^{n+1} - \mathbf{W}^*}{\Delta t} + \frac{\mathbf{F}_{i+1/2,j} - \mathbf{F}_{i-1/2,j}}{\Delta x} + \frac{\mathbf{G}_{i,j+1/2} - \mathbf{G}_{i,j-1/2}}{\Delta y} = \mathbf{Q}_{i,j}, \tag{16}$$

where $\mathbf{F}_{i\pm1/2,j} = \mathbf{F}(\mathbf{W}^*_{i\pm1/2,j})$ and $\mathbf{G}_{i,j\pm1/2} = \mathbf{G}(\mathbf{W}^*_{i,j\pm1/2})$ are the numerical fluxes at the cell interfaces $x = x_{i\pm1/2}$ and $y = y_{i\pm1/2}$, respectively. Here, $\mathbf{Q}_{i,j}$ is **a consistent discretization of the source term Q in (15) such that discretizations of the flux gradients and the source terms are well balanced, see for instance [2, 3] and further references are therein**. The spatial discretization (16) is complete when the numerical fluxes $\mathbf{F}_{i\pm1/2,j}$ and $\mathbf{G}_{i,j\pm1/2}$ along with the source term $\mathbf{Q}_{i,j}$ are reconstructed.

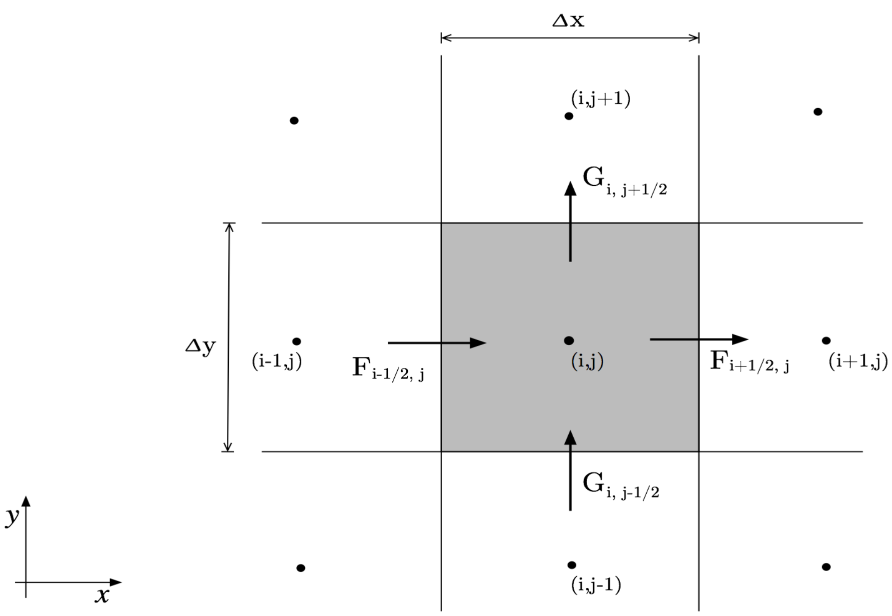

Figure 5: Illustration of the control volume $V_{i,j}$ used for the spatial discretization.

4.1 Finite volume projection procedure

In the current study, to determine the numerical fluxes in (16) we use the projection method proposed in [3]. Thus, integrating (15) over the control volume V_{ij} using the divergence theorem, we obtain

$$\begin{aligned}
\frac{\partial}{\partial t}\int_{V_{i,j}} H\ dV + \oint_{S_{i,j}} (Hun_x + Hvn_y)\ d\sigma &= 0,\\
\frac{\partial}{\partial t}\int_{V_{i,j}} Hu\ dV + \oint_{S_{i,j}} \left(\left(Hu^2 + \frac{1}{2}gH^2\right)n_x + Huvn_y\right) d\sigma &= -gH\oint_{S_{i,j}} Bn_x\ d\sigma - \xi gH^2\oint_{S_{i,j}} \bar{c}n_x\ d\sigma,\\
\frac{\partial}{\partial t}\int_{V_{i,j}} Hv\ dV + \oint_{S_{i,j}} \left(Huvn_x + \left(Hv^2 + \frac{1}{2}gH^2\right)n_y\right)\ d\sigma &= -gH\oint_{S_{i,j}} Bn_y\ d\sigma - \xi gH^2\oint_{S_{i,j}} \bar{c}n_y\ d\sigma,\\
\frac{\partial}{\partial t}\int_{V_{i,j}} H\bar{c}\ dV + \oint_{S_{i,j}} (Hu\bar{c}n_x + Hv\bar{c}n_y)\ d\sigma &= 0,
\end{aligned}$$

where $\eta = (n_x, n_y)^T$ is the unit outward normal to the surface $S_{i,j}$ of the control volume V_{ij}. Using the local cell outward normal η and tangential $\tau = \eta^\perp$ illustrated in Figure 4.1, the above equations can be projected as

$$\frac{\partial}{\partial t}\int_{V_{i,j}} H\ dV + \oint_{S_{i,j}} (Hu_\eta)\ dS = 0, \tag{17a}$$

$$\frac{\partial}{\partial t}\int_{V_{i,j}} Hu\ dV + \oint_{S_{i,j}} \left(Huu_\eta + \frac{1}{2}gH^2n_x\right)\ dS = -gH\oint_{S_{i,j}} Bn_x\ dS - \xi gH^2\oint_{S_{i,j}} \bar{c}n_x\ dS, \tag{17b}$$

$$\frac{\partial}{\partial t}\int_{V_{i,j}} Hv\ dV + \oint_{S_{i,j}} \left(Hvu_\eta + \frac{1}{2}gH^2n_y\right)\ dS = -gH\oint_{S_{i,j}} Bn_y\ dS - \xi gH^2\oint_{S_{i,j}} \bar{c}n_y\ dS, \tag{17c}$$

$$\frac{\partial}{\partial t}\int_{V_{i,j}} H\bar{c}\ dV + \oint_{S_{i,j}} (Hu\bar{c}n_\eta)\ dS = 0, \tag{17d}$$

where the normal projected velocity $u_\eta = un_x + vn_y$ and the tangential projected velocity $u_\tau = vn_x - un_y$. In order to simplify the system (17), we first sum the equation (17b) multiplied by n_x to the equation (17c)

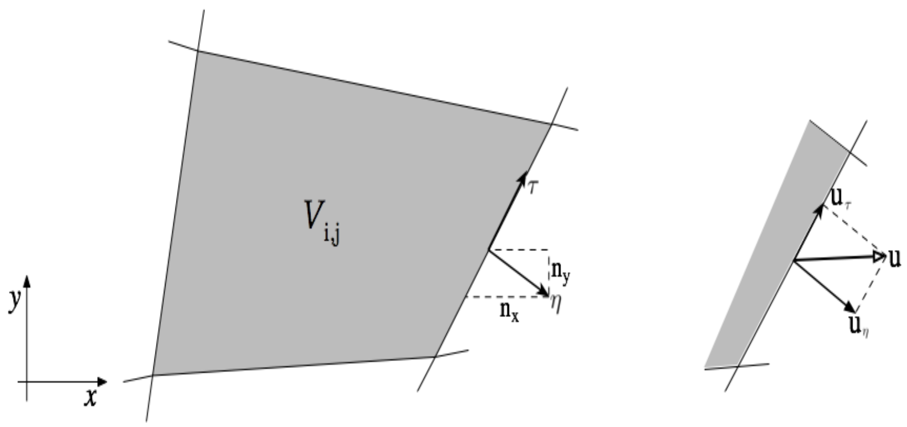

Figure 6: The projected velocities on the control volume $V_{i,j}$.

multiplied by n_y, then we subtract the equation (17b) multiplied by n_y from the equation (17c) multiplied by n_x. These operations result in

$$\begin{aligned}
\frac{\partial}{\partial t}\int_{V_{i,j}} H\, dV + \oint_{S_{i,j}} Hu_\eta\, dS &= 0,\\
\frac{\partial}{\partial t}\int_{V_{i,j}} Hu_\eta\, dV + \oint_{S_{i,j}} \left(Hu_\eta u_\eta + \frac{1}{2}gH^2\right) dS &= -gH\oint_{S_{i,j}} B\, dS - \xi g H^2 \oint_{S_{i,j}} \bar{c} n_\eta\, dS,\\
\frac{\partial}{\partial t}\int_{V_{i,j}} Hu_\tau\, dV + \oint_{S_{i,j}} Hu_\tau u_\eta\, dS &= 0,\\
\frac{\partial}{\partial t}\int_{V_{i,j}} H\bar{c}\, dV + \oint_{S_{i,j}} H\bar{c} u_\eta\, dS &= 0,
\end{aligned}$$

which can be rewritten in a differential advective form as

$$\begin{aligned}
\frac{\partial H}{\partial t} + u_\eta \frac{\partial H}{\partial \eta} + H\frac{\partial u_\eta}{\partial \eta} &= 0,\\
\frac{\partial u_\eta}{\partial t} + u_\eta \frac{\partial u_\eta}{\partial \eta} + g\frac{\partial H}{\partial \eta} &= -g\frac{\partial B}{\partial \eta} - \xi g H \frac{\partial \bar{c}}{\partial \eta},\\
\frac{\partial u_\tau}{\partial t} + u_\eta \frac{\partial u_\tau}{\partial \eta} + H\frac{\partial u_\tau}{\partial \eta} &= 0,\\
\frac{\partial \bar{c}}{\partial t} + u_\eta \frac{\partial \bar{c}}{\partial \eta} + H\frac{\partial \bar{c}}{\partial \eta} &= 0.
\end{aligned} \tag{18}$$

Introducing the total material derivative $\frac{D}{Dt}$ defined as

$$\frac{D}{Dt} = \frac{\partial}{\partial t} + u_\eta \frac{\partial}{\partial \eta}, \tag{19}$$

the system (18) can also be reformulated in a non-conservative compact vector form as

$$\frac{D\mathbf{U}}{Dt} = \mathbf{S}(\mathbf{U}), \tag{20}$$

where

$$\mathbf{U} = \begin{pmatrix} H \\ \\ u_\eta \\ \\ u_\tau \\ \\ \overline{c} \end{pmatrix}, \qquad \mathbf{S}(\mathbf{U}) = \begin{pmatrix} -H\dfrac{\partial u_\eta}{\partial \eta} \\ -g\dfrac{\partial (H+B)}{\partial \eta} - \xi g H \dfrac{\partial \overline{c}}{\partial \eta} \\ -H\dfrac{\partial u_\tau}{\partial \eta} \\ -H\dfrac{\partial \overline{c}}{\partial \eta} \end{pmatrix}. \tag{21}$$

It is worth remarking that the projection techniques reduce the solution of two-dimensional system (15) in the control volume $V_{i,j}$ to the solution of a one-dimensional system (18) on each surface $S_{i,j}$ of this control volume.

4.2 Reconstruction of the numerical fluxes

To approximate the numerical fluxes $\mathbf{F}_{i\pm1/2,j}$ and $\mathbf{G}_{i,j\pm1/2}$ in (16) we consider the modified method of characteristics applied to the projected system (18). In general, this method consists of imposing a regular grid at the new time level and backtracking the flow trajectories to the previous time level, see for instance [3]. The solutions at the old time level are obtained using interpolation from their known values on a regular grid. Hence, for each gridpoint $x_{i+1/2}$ we calculate the characteristic curves $X_{i+1/2}(s)$ associated with the particle trajectory, (20), by solving the initial-value problems

$$\begin{aligned} \frac{dX_{i+1/2}(s)}{ds} &= u_\eta\Big(s, X_{i+1/2}(s), y_j\Big), \qquad s \in [t_n, t_{n+1}], \\ X_{i+1/2}(t_{n+1}) &= x_{i+1/2}. \end{aligned} \tag{22}$$

with similar initial-value problems for the characteristic curves $Y_{j+1/2}(s)$ related to the gridpoint $y_{j+1/2}$

$$\begin{aligned} \frac{dY_{j+1/2}(s)}{ds} &= u_\eta\Big(s, x_i, Y_{j+1/2}(s)\Big), \qquad s \in [t_n, t_{n+1}], \\ Y_{j+1/2}(t_{n+1}) &= y_{j+1/2}, \end{aligned} \tag{23}$$

As shown in Figure 7, $X_{i+1/2}(s)$ and $Y_{j+1/2}(s)$ are the departure points at time s of a particle that will arrive in the time t_{n+1} at the gridpoint $x_{i+1/2}$ and $y_{j+1/2}$ respectively. In our simulations we used a second-order Runge-Kutta method for the solution of the initial-value problems (22) and (23). In general $X_{i+1/2}(t_n)$ and $Y_{j+1/2}(t_n)$ will not coincide with the spatial position of a gridpoint. Hence, once the characteristic curves $X_{i+1/2}(t_n)$ and $Y_{j+1/2}(t_n)$ are accurately calculated, the intermediate solutions $W^n_{i+1/2,j}$ and $W^n_{i,j+1/2}$ of a function W are reconstructed using

$$W^n_{i+1/2,j} = \widehat{W}^n_{i+1/2,j}, \qquad W^n_{i,j+1/2} = \widehat{W}^n_{i,j+1/2}. \tag{24}$$

Where $\widehat{W}^n_{i+1/2,j} = W\left(t_n, X_{i+1/2}(t_n), y_j\right)$ and $\widehat{W}^n_{i,j+1/2} = W\left(t_n, x_i, Y_{j+1/2}(t_n)\right)$ are the solutions at the departure points obtained by interpolation from the gridpoints of the control volume where these departure points belong, see Figure 7. Various methods of interpolation are possible, for example, a Lagrange-based interpolation polynomial can be used. Assuming that the departure points $X_{i+1/2}(t_n)$ and $Y_{j+1/2}(t_n)$ are accurately approximated, the first stage (predictor step) of the solution of the multilayer shallow water

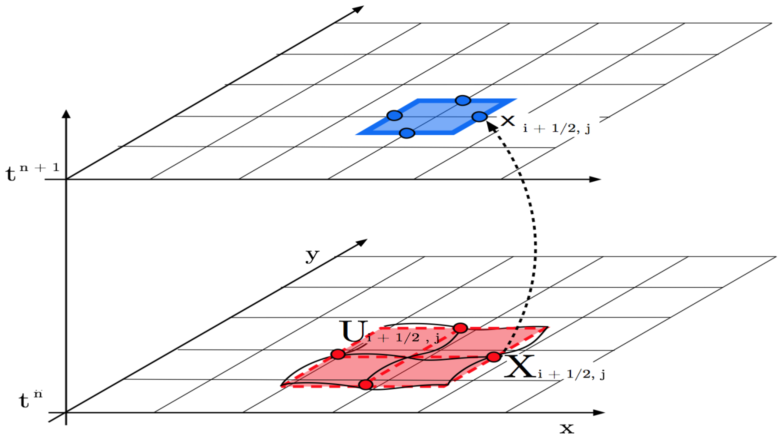

Figure 7: Sketch of the method of characteristics, where a water particle at gridpoint $x_{i+1/2}$ is backtraced through the time step to $X_{i+1/2}$.

system (5) in the Eulerian Lagrangian method is defined as

$$
\begin{aligned}
H^n_{i+1/2,j} &= \widehat{H}^n_{i+1/2,j} - \frac{\Delta t}{\Delta x}\widehat{H}^n_{i+1/2,j}\left((u_\eta)^n_{i+1,j} - (u_\eta)^n_{i,j}\right),\\
(u_\eta)^n_{i+1/2,j} &= (\widehat{u}_\eta)^n_{i+1/2,j} - g\frac{\Delta t}{\Delta x}\Big((H^n+B)_{i+1,j} - (H^n+B)_{i,j} + \widehat{\xi}^n_{i+1/2,j}\widehat{H}^n_{i+1/2,j}\left(c^n_{i+1,j} - c^n_{i,j}\right)\Big),\\
(u_\tau)^n_{i+1/2,j} &= (\widehat{u}_\tau)^n_{i+1/2,j} - \frac{\Delta t}{\Delta x}\widehat{H}^n_{i+1/2,j}\left((u_\tau)^n_{i+1,j} - (u_\tau)^n_{i,j}\right),\\
c^n_{i+1/2,j} &= \widehat{c}^n_{i+1/2,j} - \frac{\Delta t}{\Delta x}\widehat{c}^n_{i+1/2,j}\left((u_\eta)^n_{i+1,j} - (u_\eta)^n_{i,j}\right),
\end{aligned}
\tag{25}
$$

where

$$
\widehat{H}^n_{i+1/2,j} = H\left(t_n, X_{i+1/2}(t_n), y_j\right), \qquad (\widehat{u}_\eta)^n_{i+1/2,j} = u_\eta\left(t_n, X_{i+1/2}(t_n), y_j\right),
$$
$$
(\widehat{u}_\tau)^n_{i+1/2,j} = u_\tau\left(t_n, X_{i+1/2}(t_n), y_j\right), \qquad \widehat{c}^n_{i+1/2,j} = c\left(t_n, X_{i+1/2}(t_n), y_j\right).
$$

The intermediate states in the y-direction $H^n_{i,j+1/2}$, $(u_{\alpha,\eta})^n_{i,j+1/2}$ and $(u_{\alpha,\tau})^n_{i,j+1/2}$ are calculated in the same way. When the projected states calculations are complete, the states $\mathbf{W}^n_{i\pm1/2,j}$ and $\mathbf{W}^n_{i,j\pm1/2}$ are determined by using $v_\alpha = (u_{\alpha,\tau}, u_{\alpha,\eta})\cdot\eta$ and $u_\alpha = (u_{\alpha,\tau}, u_{\alpha,\eta})\cdot\tau$.

Using the concept of C-property the discretization of the source terms $\mathbf{Q}_{i,j}$ is carried so that the discretized source terms are well balanced with the discretized flux gradients, for further explanation see [3]. The source terms are thus reconstructed, such that the condition is preserved after discretization. For one-dimensional shallow water equations, the terms are discretized as follows

$$
\begin{aligned}
\left(gH\frac{\partial B}{\partial x}\right)^n_{i,j} &= g\frac{H^n_{i+1/2,j} + H^n_{i-1/2,j}}{2}\frac{B^n_{i+1,j} - B^n_{i-1,j}}{2\Delta x},\\
\left(gH\frac{\partial B}{\partial y}\right)^n_{i,j} &= g\frac{H^n_{i,j+1/2} + H^n_{i,j-1/2}}{2}\frac{B^n_{i,j+1} - B^n_{i,j-1}}{2\Delta y},
\end{aligned}
\tag{26}
$$

where the averaged solutions are defined by

$$
H^n_{i+1/2,j} = \frac{H^n_{i+1,j} + H^n_{i-1,j}}{2}, \qquad H^n_{i,j+1/2} = \frac{H^n_{i,j+1} + H^n_{i,j-1}}{2}.
$$

By projecting the original shallow water model into the local system and using dimension-by-dimension discretization, the source terms (26) can be discretized as shown.

Table 1: Sediment parameters reported in [35, 39, 27] for some bed types used in our simulations for the erosion and deposition formulae.

Bed type	d $[mm]$	p	φ	ω_s $[m/s]$	ρ_s $[kg/m^3]$
Sand 1	0.0625	0.5	0.015	0.00014	1650
Sand 2	0.25	0.35	0.015	0.001	1600
Sand 3	1	0.25	0.015	0.002	1520
Sediment 1	0.5	0.42	0.00015	0.2	2630
Sediment 2	1.61	0.42	0.00015	0.2	2630
Sediment 3	2	0.42	0.00015	0.2	2630
Pearls	6.1	0.4	0.000015	0.0001	1048

5 Numerical results and examples

Several test examples for shallow water flows over multilayer movable beds are presented in this section to ascertain the accuracy and adaptability of the proposed techniques. We also compare numerical results obtained using our approach to experimental data for two examples. Dam-break flow problems are presented to illustrate the performance of the proposed numerical solver combined with the discretized bed in resolving non-homogeneous erodible sediment beds. We present computational results for both single-layer and three-layer beds using the sediment characteristics listed in Table 1. These sediment parameters have been recommended in many experimental studies on sediment transport applications, see for instance [35, 39, 27]. In our simulations, $\rho_w = 1000\ kg/m^3$, $g = 9.81\ m/s^2$ and $\nu = 1.2 \times 10^{-6}\ m^2/s$. **In addition, because of the considered splitting procedure (14)-(15), a consistent Courant number of $Cr = 0.8$ is used to adjust the timestep Δt according to the stability condition**

$$\Delta t = \mathrm{Cr}\frac{\min(\Delta x, \Delta y)}{\max\limits_{k=1,\ldots,5}\left(|\lambda_k^n|, |\mu_k^n|\right)}, \tag{27}$$

where λ_k and μ_k $(k = 1, \ldots, 5)$ are the eigenvalues of the sediment transport system given in (3). It should be pointed out that the stability condition (27) accounts for the rate of vertical changes and thus it also ensures that the bed-load never travels more than one control volume as long as the vertical discretization step $\Delta z \leq \min(\Delta x, \Delta y)$.

5.1 Rectangular dam-break flows over erodible beds

In this class of flow problems, we consider a dam-break problem in a squared channel of length 20 m with a three-layer bed initially assumed to be flat. At time $t = 0$, the flow is assumed to be at rest and

$$H(0,x,y) = \begin{cases} 2\ m, & \text{if} \quad x \leq 0, \\ 0.2\ m, & \text{if} \quad x > 0, \end{cases} \qquad \bar{c}(0,x,y) = 0.0001, \quad u(0,x,y) = v(0,x,y) = 0.$$

The depth of the bed is 0.3 m with three layers initially formed by

$$B(0,x,y,z) = \begin{cases} \text{Sand 1}, & \text{if} \quad -0.15\ m \leq z < 0\ m, \\ \text{Sand 2}, & \text{if} \quad -0.3\ m \leq z < -0.15\ m, \\ \text{Sand 3}, & \text{if} \quad -1.0\ m \leq z < -0.3\ m. \end{cases}$$

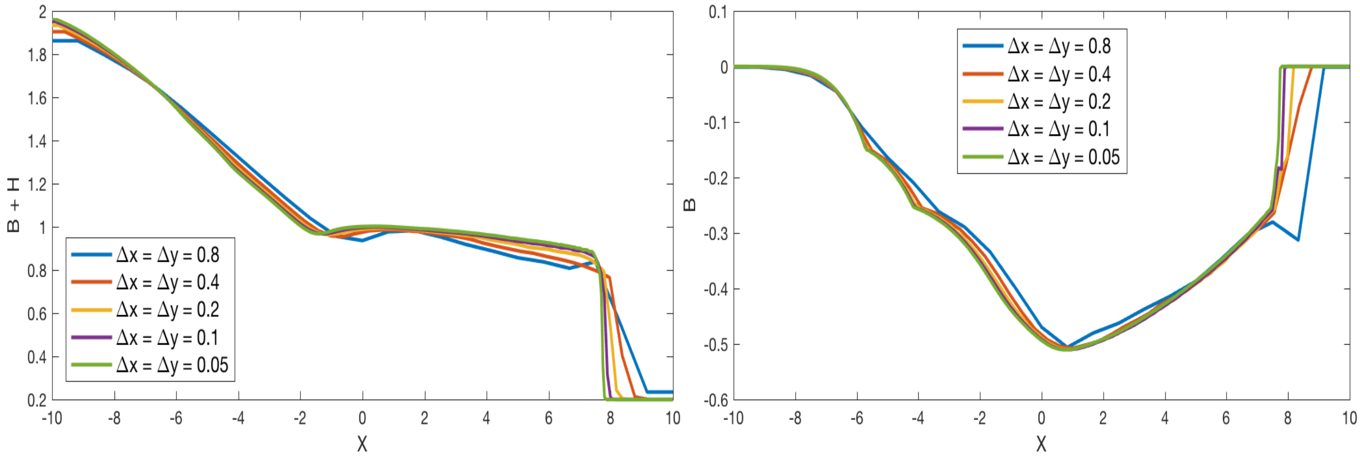

Figure 8: Water height (left) and bed profile (right) obtained for the test example of rectangular dam-break over a three-layer bed at time $t = 2\ s$ using different meshes.

The sediment properties of Sand 1, Sand 2 and Sand 3 are listed in Table 1. This example is considered to perform mesh convergence in the proposed multilayer model using different numbers of control volumes in the spatial discretization. Figure 8 depicts the computational results for the water height and the bed-load obtained at time $t = 2\ s$ using $\Delta z = 0.1\ m$ and different values of $(\Delta x, \Delta y)$. **It is clear from these results that refining the horizontal mesh results in a convergence for both water heights and bed profiles obtained using the FVC method.** In order to quantify the errors in these results, we summarize in Table 2 the errors in the bed-load, errors in the minimum values of the bed profile, and the computational times for different mesh discretizations of $(\Delta x, \Delta y, \Delta z)$. Here, a reference solution computed using a fine discretization with $\Delta x = 0.025\ m$, $\Delta y = 0.025\ m$ and $\Delta z = 0.001\ m$ is used as an analytical solution. The L^1-norm is used to compute the errors, and results are present at the final time $t = 2\ s$. It is clear from the results presented in Table 2 that increasing the number of control volumes in the horizontal spatial discretization yields an increase in the accuracy and also in the computational cost of the FVC method. Using the coarse discretization $(\Delta x = \Delta y = 0.8\ m, \Delta z = 0.2\ m)$, the computed errors for the water height and the bed profile are more pronounced than for the other discretizations. It should also be noted that, when compared to the lateral discretization, the vertical discretization has small effects on both the accuracy and the efficiency of the proposed model. For instance, for a simulation using $(\Delta x = \Delta y = 0.4\ m, \Delta z = 0.1\ m)$ the computational time and the errors in the bed profile and the minimum values of the bed profile are $69.47\ s$, $6.44\ \%$ and $7.19\ \%$, respectively. By contrast, a discretization of $(\Delta x = \Delta y = 0.1\ m, \Delta z = 0.025\ m)$ reduces the errors in the bed profile and the minimum values of the bed profile respectively to $1.65\ \%$ and $0.10\ \%$, which is a substantial improvement in accuracy. For this later simulation with $(\Delta x = \Delta y = 0.1\ m, \Delta z = 0.025\ m)$ the computational times increases to $8384\ s$. It is evident that for this test example, a mesh convergence is achieved in our FVC method for both lateral and vertical discretizations. For the considered flow and sediment conditions, a balance between accuracy and efficiency in the FVC method favored the vertical discretization using $\Delta z = 0.025\ m$. **It should also be pointed out that in this study the speed of bed evolution is about an order of magnitude slower than that of the water flow, thus the bed has a different vertical and horizontal discretizations.**

5.2 Circular dam-break flows over erodible beds

Next, we consider test examples for circular dam-break flows over erodible beds formed of single-layer and three-layer sediments. The circular dam-break problem is solved in a squared domain $[-10, 10] \times [-10, 10]$

Table 2: CPU times, errors in the bed-load, and errors in the minimum values of the bed profile using different spatial and bed discretization steps (Δx, Δy) and Δz for the test example of rectangular dam-break over three-layer bed.

Vertical discretization	Lateral discretization: $\Delta x = \Delta y = 0.8\ m$	$\Delta x = \Delta y = 0.4\ m$	$\Delta x = \Delta y = 0.2\ m$	$\Delta x = \Delta y = 0.1\ m$	$\Delta x = \Delta y = 0.05\ m$
$\Delta z = 0.2\ m$	$9.268\ s$	$69.09\ s$	$656.6\ s$	$8381\ s$	$21720\ s$
	7.68 %	6.84 %	7.17 %	7.58 %	7.63 %
	5.15 %	7.13 %	6.92 %	6.65 %	6.28 %
$\Delta z = 0.1\ m$	$8.539\ s$	$69.47\ s$	$656.5\ s$	$8387\ s$	$21650\ s$
	7.17 %	6.44 %	6.30 %	6.59 %	6.98 %
	5.32 %	7.19 %	6.98 %	6.69 %	6.38 %
$\Delta z = 0.05\ m$	$8.540\ s$	$69.16\ s$	$656.7\ s$	$8388\ s$	$25260\ s$
	2.36 %	1.58 %	1.50 %	1.99 %	2.56 %
	1.83 %	3.59 %	3.25 %	3.06 %	2.84 %
$\Delta z = 0.025\ m$	$8.530\ s$	$69.10\ s$	$657.3\ s$	$8384\ s$	$24180\ s$
	1.27 %	2.31 %	2.20 %	1.65 %	1.19 %
	0.79 %	0.38 %	0.21 %	0.10 %	0.29 %
$\Delta z = 0.0125\ m$	$10.84\ s$	$74.03\ s$	$664.7\ s$	$8413\ s$	$23110\ s$
	4.07 %	2.61 %	3.48 %	1.98 %	0.92 %
	2.50 %	1.08 %	0.54 %	0.26 %	0.08 %

with a flat bed and subject to the following initial conditions

$$H(0,x,y) = 1 + \ 2\left(1 - \tanh\left(10\left(\sqrt{0.4x^2 + 0.4y^2} - 1\right)\right)\right), \quad u(0,x,y) = v(0,x,y) = 0. \tag{28}$$

A similar problem has been considered in [19] for the standard circular dam-break problem over a fixed bed. Hence, as a first run for this class of problems, we solve the same example on fixed bed and compare the results obtained using the FVC method to other well-established finite volume methods. **For comparison reason, we consider the first-order Riemann-based Roe solver and the Rusanov method.** In Figure 9, we present the radial cross-sections of the water height at $y = 0$ using the considered methods at time $t = 2\ s$ on two meshes with 50×50 and 100×100 cells. For comparison we also include in this figure a reference solution obtained on fine mesh with 500×500 cells. **As expected, the numerical diffusion is very pronounced in the solutions computed using the Rusanov scheme.** This excessive numerical dissipation has been reduced in the water heights using the Roe method, but the results obtained using the FVC method remain the best. In terms of computational cost, the FVC method is about 86 times faster than the Roe scheme for the same simulation. For this test example, the FVC method accurately solves the front propagation without generating nonphysical oscillations or excessive numerical dissipation in the computed results.

Our next concern with this test example is to simulate circular dam-break flows over erodible beds. To this end, we run the same simulations as in the previous test example but over a single-layer bed of depth $0.25\ m$ and formed of Sand 2, the sediment properties of which are given in Table 1. The initial conditions are the same as (28) and the sediment concentration is set to $\overline{c}(0,x,y) = 0.01$. Figure 10 depicts the results

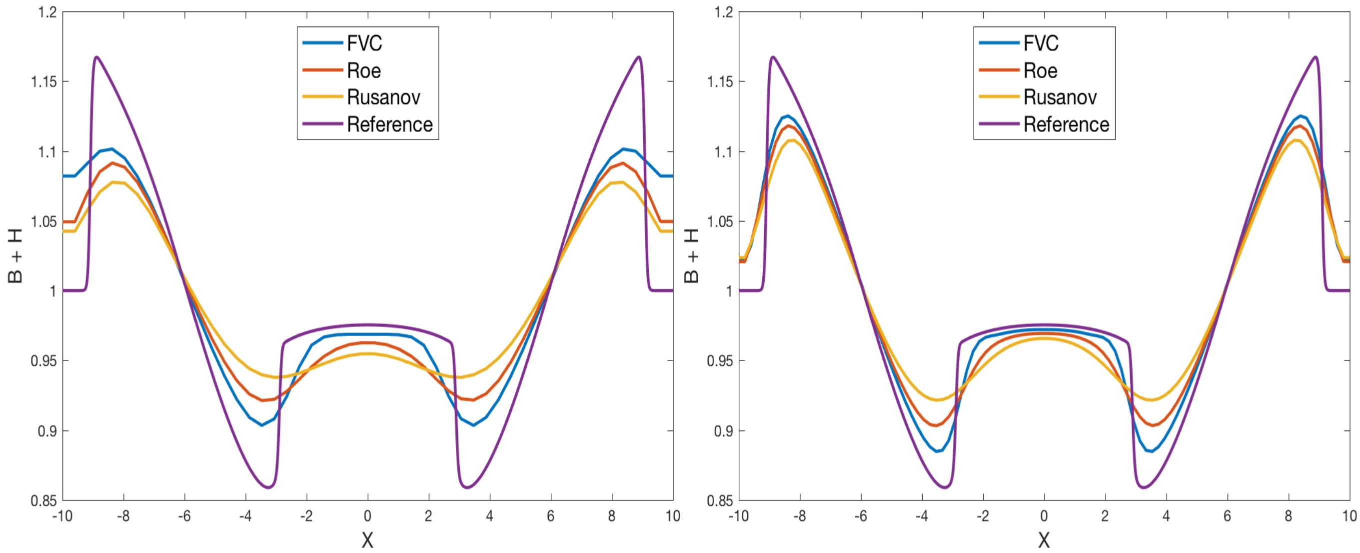

Figure 9: Comparison results for radial cross-sections of the water height obtained using different finite volume methods for the test example of circular dam-break over a fixed single-layer bed at time $t = 2\ s$ using $\Delta x = \Delta y = 0.4$ (left) and $\Delta x = \Delta y = 0.2$ (right).

obtained for the water height, bed-load, and sediment concentration obtained on a mesh with 100×100 at three different times. Here, only radial cross-sections at $y = 0$ of the sediment concentration are displayed in Figure 10. It is clear that allowing for a movable bed the circular dam-break flows result in a radial erosion of the bed. From the presented results it is also clear that the water flows away from the central region, as the rarefaction wave propagates outwards. Note that the FVC method has accurately resolved this dam-break flow and it fully preserves the radial symmetry in all flow and sediment variables.

To emphasis the effects of multilayer bed on this dam-break problem, we perform the same simulations on a bed 30 cm deep and comprised of three layers as

$$B(0,x,y,z) = \begin{cases} \text{Sand 1,} & \text{if} \quad -0.05\ m \ \le z < \ 0\ m, \\ \text{Sand 2,} & \text{if} \quad -0.1\ m \ \le z < \ -0.05\ m, \\ \text{Sand 3,} & \text{if} \quad z < \ -0.1\ m, \end{cases}$$

and the initial sediment concentrations are $\overline{c}(0,x,y) = 0.01$, $c_1(0,x,y) = 0.01$. The sediment parameters for Sand 1, Sand 2 and Sand 3 are given in Table 1. Notice that, since the highly erodible Sand 1 is used in this test example, one expects to see more net erosion in the bed as well as a different concentration profile compared to the previous test example of single-layer bed. The central bed peak should also be retained in this case, along with a bed that reflects the differences in erosion profiles of the multiple sedimentary sands. In Figure 11, we present the water height, bed-load and radial cross-section of the sediment concentrations obtained a mesh with 100×100 gridpoints, using vertical discretization $\Delta z = 0.005m$ at three different instants. Again, a perfect symmetry is obtained using our FVC method for this dam-break problem over a three-layer sedimentary bed. Compared to the results obtained for the single-layer bed in Figure 10, the results for the three-layer bed in Figure 11 show roughly the same quantity of scour, though the crucial difference lies in the erosion rate for each simulation, compare the concentration profiles in Figure 10 and Figure 11. For instance, it is noticeable that Sand 1, with its higher erosion rate, causes a greater net scour, whereas between the two simulations, Sand 2 has a roughly constant sediment concentration rate from $t = 0.5\ s$ onwards. This implies that only the initial wave speed was large enough to cause the scour of sand 2 in the bed. The computed results for this example of circular dam-break flows over erodible

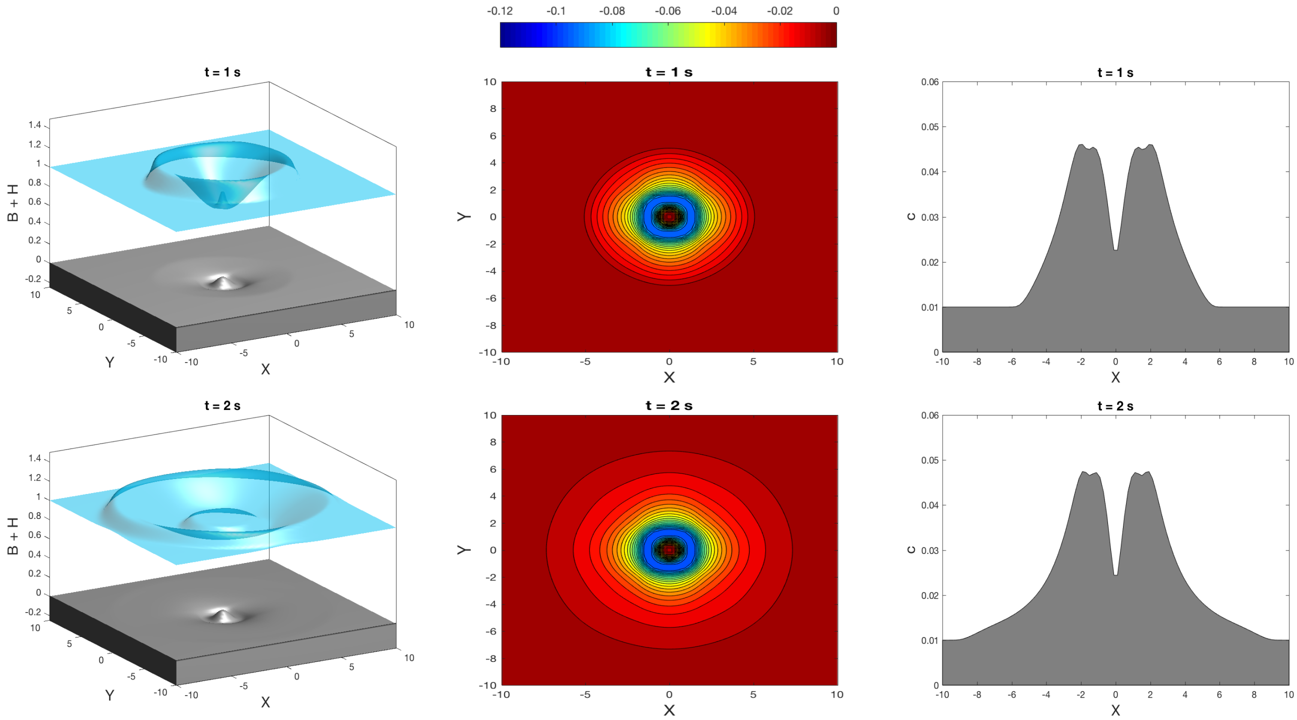

Figure 10: Results obtained for the free-surface (first column), bed-load (second column) and cross-section of the sediment concentration at $y = 0\ m$ (third column) for the circular dam-break over a single-layer sediment erodible bed at $t = 1\ s$ (first row) and $t = 2\ s$ (second row).

beds have demonstrated the ability of the FVC method to handle multiple sediments in the beds. Here, the proposed model combined with the FVC method is able to accurately resolve the erosion effects in multilayer sedimentary beds, as well as to capture the multiple sediment concentrations which are vital to the understanding of sediment transport presented by this class of dam-break problems.

5.3 Partial dam-break flows over erodible beds

The aim of this class of test examples is to investigate the effects of multiple sediment layers on partial dam-break flows over movable beds. Here, we solve the system (5) in a 200 m long and 200 m wide flat reservoir with two different constant water levels separated by a dam. At $t = 0$ part of the dam breaks instantaneously. The dam is 4 m thick and the breach is assumed to be 75 m wide. In the first run for this class of test problems we assume the bed is flat and initially, $B(0, x, y) = 0$,

$$H(0,x,y) = \begin{cases} 5\ m, & \text{if} \quad x \leq 100\ m, \\ 0.5\ m, & \text{if} \quad x > 100\ m, \end{cases} \qquad \bar{c}(0,x,y) = c_1(0,x,y) = 0.0001, \quad u(0,x,y) = v(0,x,y) = 0. \quad (29)$$

In all our simulations for this dam-break problem, the computational domain is discretized into 100×100 control volumes **with a uniform discretization of $\Delta x = \Delta y = 2\ m$**. Note that this test example has been widely used in the literature for the assessment of numerical methods for dam-break problems on both fixed beds and single-layer erodible beds, see for example [12, 40, 37, 6, 2]. At time $t = 0$ the dam breaks asymmetrically and the water propagates downstream developing a shock wave while spreading laterally.

We first solve this test problem over a single-layer bed 6 m deep formed of Sand 2, see Table 1 for the sediment parameters associated with this bed. The initial conditions are given in (29) and the sediment

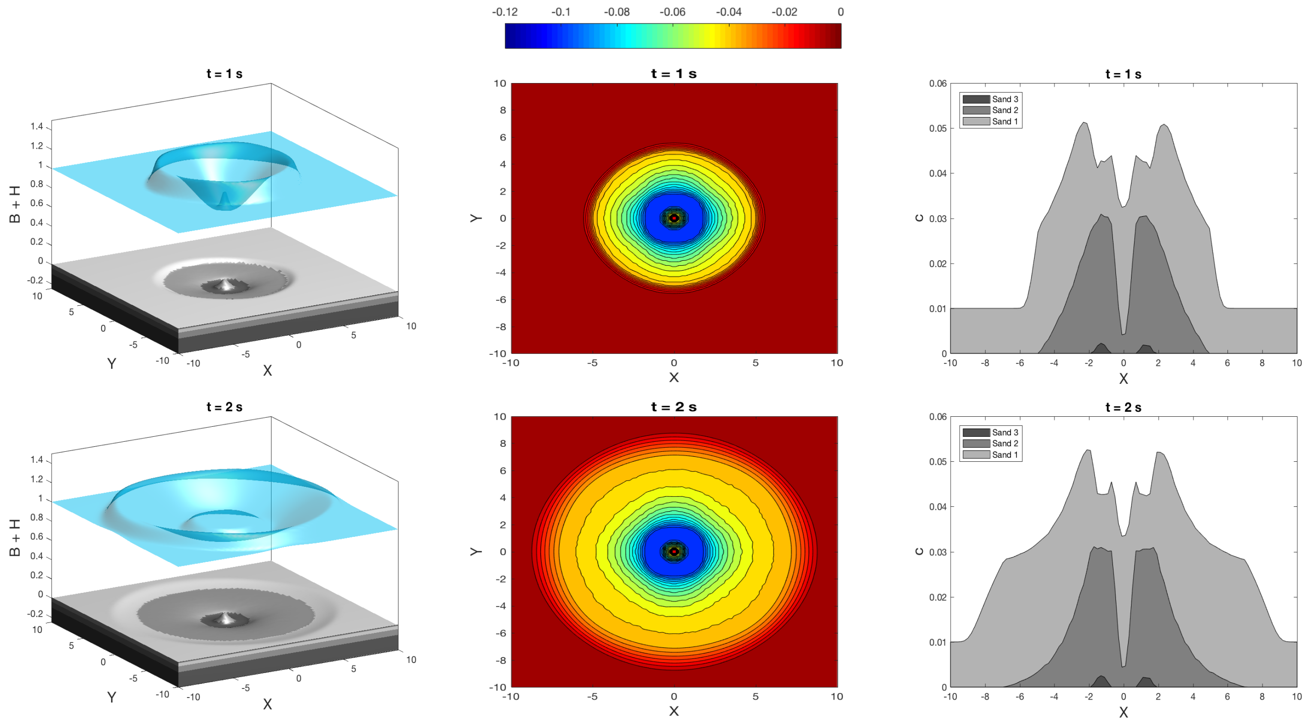

Figure 11: Same as Figure 10 but for the circular dam-break over a three-layer sediment erodible bed.

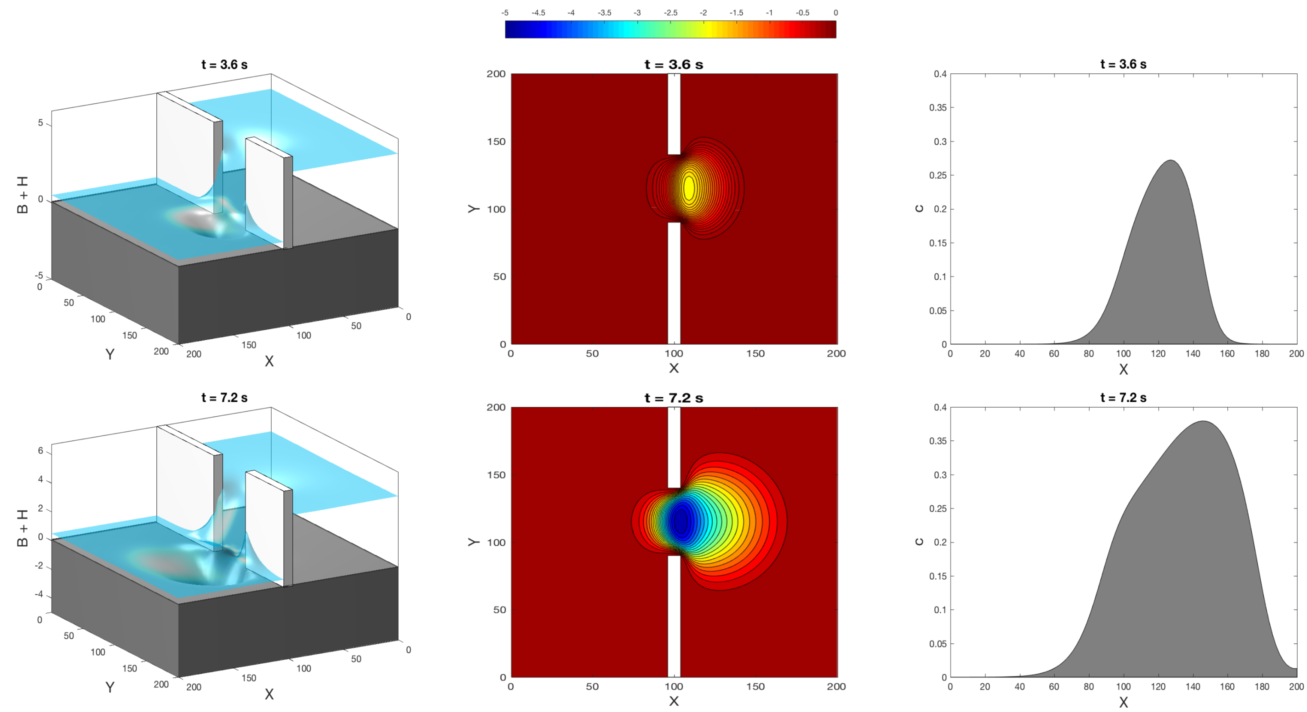

Figure 12: Results obtained for the free-surface (first column), bed-load (second column) and cross-section of the sediment concentration at $y = 0$ m (third column) for the partial dam-break over a single-layer sediment erodible bed at $t = 3.6$ s (first row) and $t = 7.2$ s (second row).

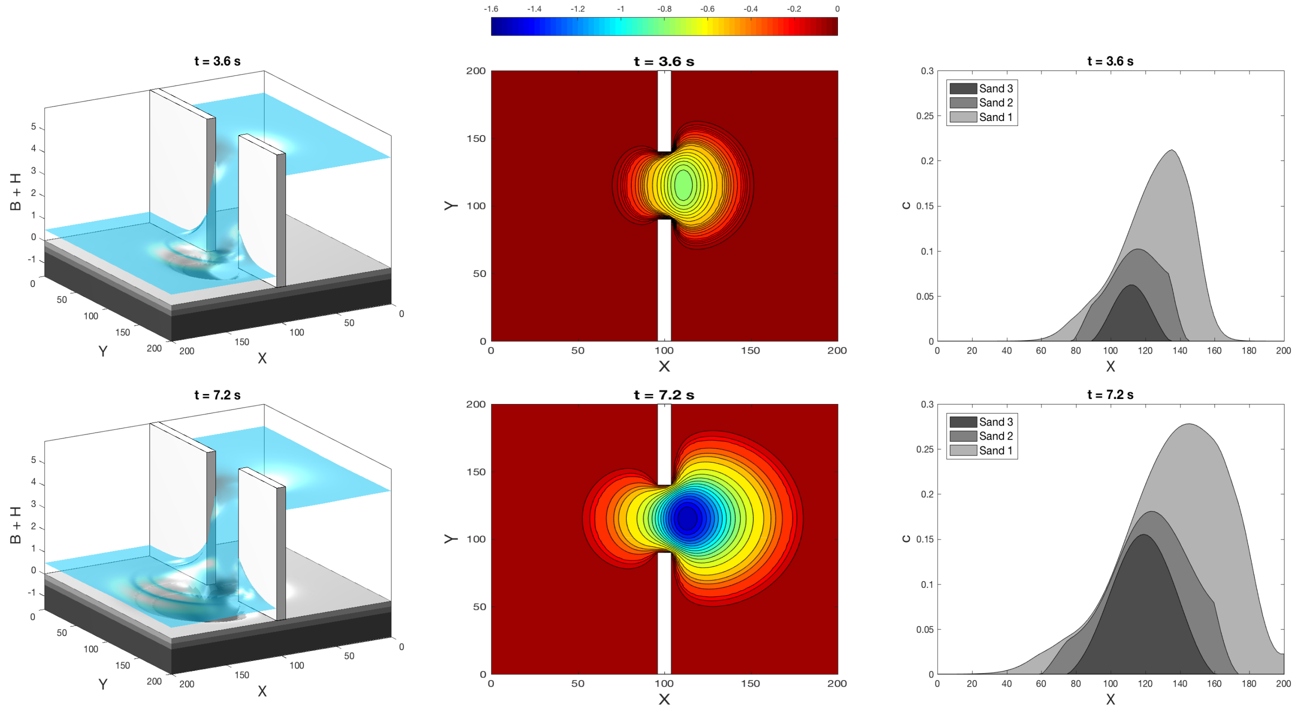

Figure 13: Same as Figure 12 but for the partial dam-break over a three-layer sediment erodible bed.

concentration is initially set to $\overline{c}(0, x, y) = 0.0001$. The water height, bed-load and cross-sections of the sediment concentration at $y = 100\ m$ are presented in Figure 12 at three different times. Under the considered flow and sediment conditions, we can observe in these results that the right moving flow propagates to the downstream whereas, the rarefaction wave propagates to the upstream generating a deep erosion at the dam breach. It is clear that the water free-surface obtained for the dam-break on the erodible bed shows different features to those obtained for dam-break on the fixed bed. Notice that the erosion is more pronounced at the breach because of the large velocity field in this area. Our results are similar to other results presented in [2]. As can be observed from these results, the dam-break flow over the movable bed can build up a heavily concentrated wavefront which is bounded by the wave forefront and a contact discontinuity of the sediment transport, and that it depresses in the long run. The bed mobility can strongly modify the water free-surface profiles and may have considerable implications for flood predictions. As in the previous simulations, an hydraulic jump in the water free-surface is initially formed around the dam site. It depresses progressively as it propagates upstream and eventually disappears. It is evident that the movable bed can be significantly scoured and the dimensions of the scour hole are of a similar order of magnitude to those of the water flow itself. Therefore the rate of bed deformation is not negligible compared to that of the flow change, characterizing the need for coupled modelling of the strongly interacting flow-sediment-morphology system, as considered in the present work. From the presented results, we can conclude that the proposed FVC method performs very well for this dam-break problem since it does not diffuse the moving water fronts and no spurious oscillations have been detected when the dam breaks over the sedimentary bed.

Our next concern is to demonstrate the capability of the proposed model in dealing with a multilayer bed on this partial dam-break problem. Here, we consider the same simulations on a 2 m deep bed formed

Table 3: Comparison results for the total water discharge and the disturbed area obtained at four different instants for the partial dam-break over fixed, single-layer and three-layer beds.

		t = 1.8 s	t = 3.6 s	t = 5.4 s	t = 7.2 s
Fixed bed	Total discharge $[m^3]$	1788	3204	5012	6493
	Disturbed area $[m^2]$	1316	2322	3380	4169
Single-layer bed	Total discharge $[m^3]$	1877	3589	5884	8488
	Total suspended sediment $[m^3]$	260	1435	3570	6312
	Disturbed area $[m^2]$	2877	5367	8399	11848
Three-layer bed	Total discharge $[m^3]$	2005	3463	5058	6681
	Total suspended sediment $[m^3]$	413	1150	2203	3471
	Percentage of Sand 1 [%]	66.8	61.3	58.2	56.3
	Percentage of Sand 2 [%]	31.7	26.6	22.5	20.4
	Percentage of Sand 3 [%]	1.6	12.1	19.3	23.2
	Disturbed area $[m^2]$	3126	5910	9170	12840

with three layers as

$$B(0,x,y,z) = \begin{cases} \text{Sand 1,} & \text{if} \quad -0.25\,m \ \le z < \ 0\,m, \\ \text{Sand 2,} & \text{if} \quad -0.5\,m \ \le z < \ -0.25\,m, \\ \text{Sand 3,} & \text{if} \quad -2.0\,m \ \le z < \ -0.5\,m, \end{cases}$$

and the initial sediment concentrations are $\bar{c}(0,x,y) = 0.001$ and $c_1(0,x,y) = 0.001$. The sediment parameters for Sand 1, Sand 2 and Sand 3 are given in Table 1. **A uniform vertical discretization with $\Delta z = 0.025\ m$ is used in our simulations.** The three-layer sediment model provides good results with a clear difference in bathymetry as shown in Figure 13 compared to Figure 12. This ability to handle multiple sediments allows analysis of erosion over a greater area highlighting the more easily eroded Sand 1 whereas, capturing the limitation on net erosion caused by the base layer formed by the less easily eroded Sand 3. Note that as Sand 2 is an average of Sand 1 and Sand 3, it is possible to compare the results for single and three-layer beds and note the differences. It is also easy to see in Figure 12 the excess erosion caused by a single-layer sediment assumptions. It should be noted that over-erosion is a common problem for this type of simulations. Again, the FVC method performs well for this test example and exhibits the expected flow structures in the computational domain without requiring finite volume Riemann solvers nor very fine meshes.

The differences between the three simulation types are further inspected in Table 3. In this table, we present (i) the total discharge measured as the quantity of water evacuated from the upstream to the downstream of the dam, (ii) the disturbed area which is the area where the water height varies from the initial state *i.e.*, the area that has been disturbed by the dam break, and (iii) the total suspended sediment which is the volume taken up by the suspended sediment in the whole domain. These results are presented in Table 3 at four different instants. It is interesting to note that the erodible beds have a greater discharge than the fixed bed although they lose momentum by picking up sediment. This is mainly due to the evolving bathymetry both in front and behind the dam location as more water is accelerated through the dam. It is also interesting to note that the perturbation caused by the dam-break spreads over a far larger area than for the situation with fixed bed. This can also be attributed to the characteristics of the sediment used in the bed and to the fast water wavefront passing through the dam. Table 3 also shows the evolution of

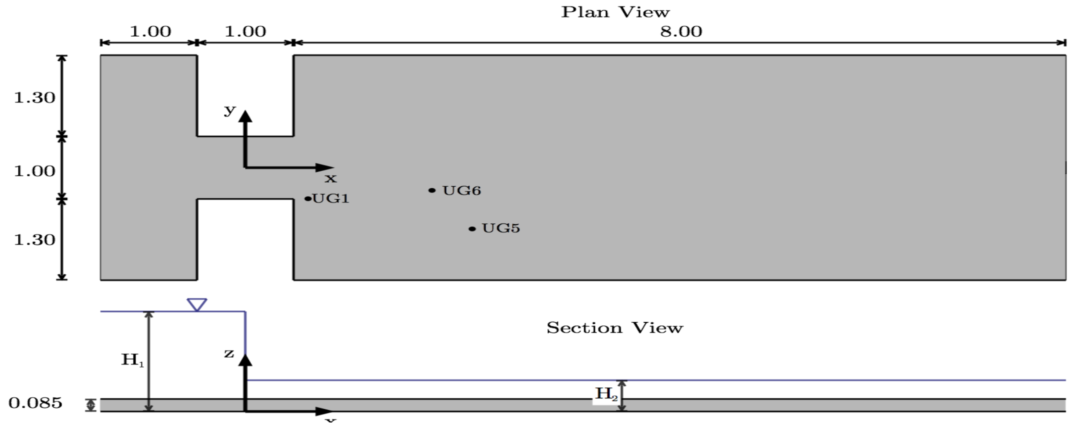

Figure 14: Configuration used for the test example of dam-break flows over mobile beds. Dimensions are given in meters and gauges used for comparison to experiments are also allocated.

sediment proportions for the three-layer erodible bed and it is interesting to see how they change over time as the various layers are eroded. Under the considered sediment conditions, the erosion of top layer in the bed decreases and while it increases for the bottom layer as time evolves. For instance at time $t = 1.8$ s the composition of the total eroded sediments contains 66.8% of Sand 1, 31.7% of Sand 2 and 1.6% of Sand 3 and at time $t = 7.2$ s these proportions become 56.3%, 20.4% of Sand 2 and 23.2% of Sand 3, respectively. It is clear that the proposed techniques are able to model multiple sediments in the bed very well.

5.4 Dam-break flows over mobile beds

Our final test example consists of a dam-break over mobile bed designed for experimental study conducted at the Université Catholique de Louvain in Belgium, and results of which are reported in [29]. Here, we solve the problem for a single-layer bed formed of Sediment 2 with its characteristics given in Table 1. A variety of measurements were taken for the bed and reported in [29] including the final distributions of the bed-load in two dimensions and also the time evolution of the water heights at three gauges in the flow domain. The configuration of the domain and its geometry along with the location of gauges are displayed in Figure 14. Initially the bed is flat and

$$H(0, x, y) = \begin{cases} H_1, & \text{if} \quad x \leq 0, \\ H_2, & \text{if} \quad x > 0. \end{cases}$$

As in [29], two situations are considered in this section namely, a quasi-dry case ($H_1 = 0.47$ m and $H_2 = 0.085$ m) and a wet case ($H_1 = 0.51$ m and $H_2 = 0.15$ m). A mesh with 200×72 elements has been used in our simulations for both test cases.

The computed bed distributions for the quasi-dry case and the wet case at time $t = 20$ s are depicted in Figure 15. As can be seen, smooth results are obtained for the wet case compared to the quasi-dry case. A deeper erosion is detected for this later case and a wider area in the computational domain is affected by the erosion than in the wet case. It is expected to observe large erosion in this class of dam-break problems for high value of the ratio H_1/H_2. Obviously, the computed results verify the stability and the shock capturing properties of the FVC method. To further examine the accuracy of the numerical model we present in Figure 16 time evolution of the water free-surface at the gauges UG1 and UG6 for the quasi-dry conditions. Time evolution of the water free-surface at the gauges UG1 and UG5 for the wet conditions is shown in Figure 17. Here, the gauges UG1, UG6 and UG5 are localized at $(0.640, -0.500)$, $(1.940, -0.330)$ and $(2.340, -0.990)$, respectively. The agreement between the simulations and measurements in these figures

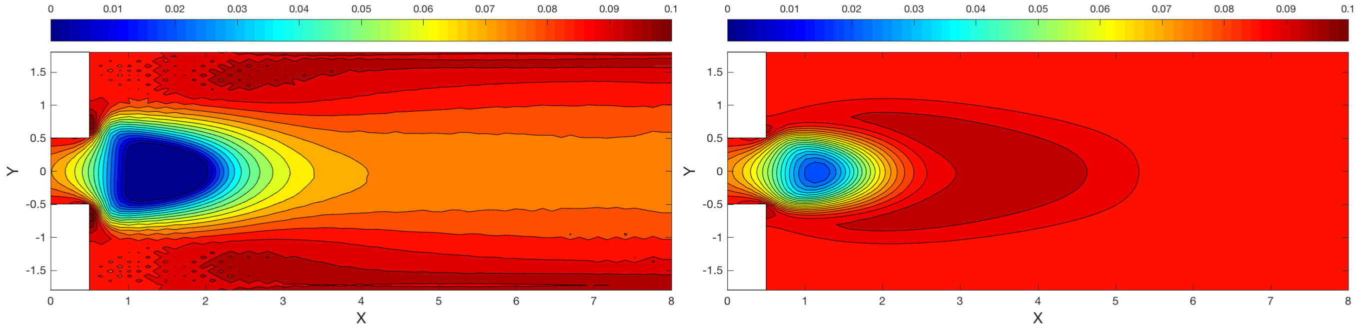

Figure 15: Bed profile at time $t = 20\ s$ for the dam-break over mobile bed using quasi-dry conditions (left plot) and wet conditions (right plot).

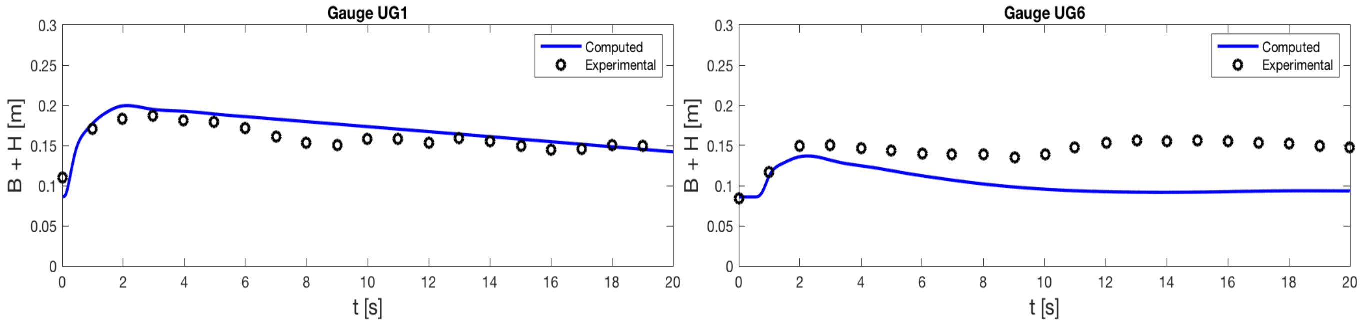

Figure 16: Time evolution of the water free-surface at the gauge UG1 (left plot) and the gauge UG6 (right plot) for the dam-break over mobile bed using quasi-dry conditions.

is fairly good. The free-surface amplitude and the erosion magnitude are well predicted by the numerical model. As expected, a hydraulic jump is formed near the initial dam location and it propagates upstream. The location of the hydraulic jump is accurately predicted by the numerical model for both wet and quasi-dry situations. However, for the quasi-dry case the numerical model slightly overpredicts the scour caused by the dam-break at the gauge UG6, compare the right plot in Figure 17. **To overcome the zero speeds in the FVC method, we perturb these speeds by 10^{-7} far from zero. Overall, the FVC method appears to perform very well for this example and it captures the correct predictions for both water free-surface and sediment transport.** It is worth remarking that as stated in [30], numerical models appear to either have good flow or scour predictions but the presented results are encouraging as we have obtained reasonable results for the bed-load and very good flow predictions.

We now turn our attention to simulations using a bed with mixed sediments. **Note that although not explicitly in the mathematical formulation, armoring and hiding are accounted for in this example by the discretization of the bed and the multimode handling of sediments.** First we consider a bed with mixed sediments to check the effects of differing sediments on the flow and bed-load features. Recall that the bed composition used in the laboratory experiment consisted of a well-graded sediment of average diameter $1.61 \times 10^{-3}\ m$ (Sediment 2 in Table 1). In this simulation, we add two variants to the sediment mixture by varying the sediment diameter d while keeping all other variables the same. We create a sand-bed using one third of Sediment 1 with $d = 0.5 \times 10^{-3}\ m$, one third of Sediment 2 with $d = 2 \times 10^{-3}\ m$, and one third of Sediment 3 with $d = 1.61 \times 10^{-3}\ m$ *i.e.*,

$$B(0, x, y, z) = \frac{1}{3}\text{Sediment } 1 + \frac{1}{3}\text{Sediment } 2 + \frac{1}{3}\text{Sediment } 3, \qquad \text{if} \qquad 0\ m\ \leq z <\ 0.085\ m.$$

The remaining parameters for these sediments are the same as listed in Table 1. We run the simulation

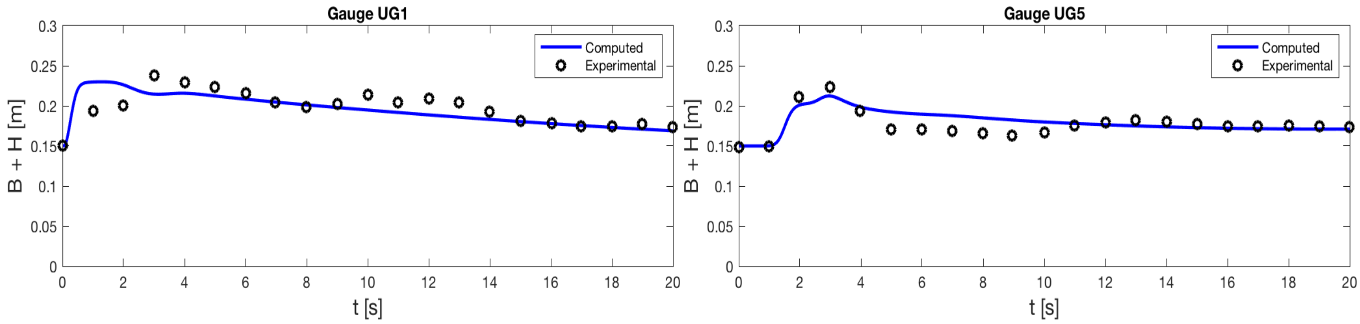

Figure 17: Time evolution of the water free-surface at the gauge UG1 (left plot) and the gauge UG5 (right plot) for the dam-break over mobile bed using wet conditions.

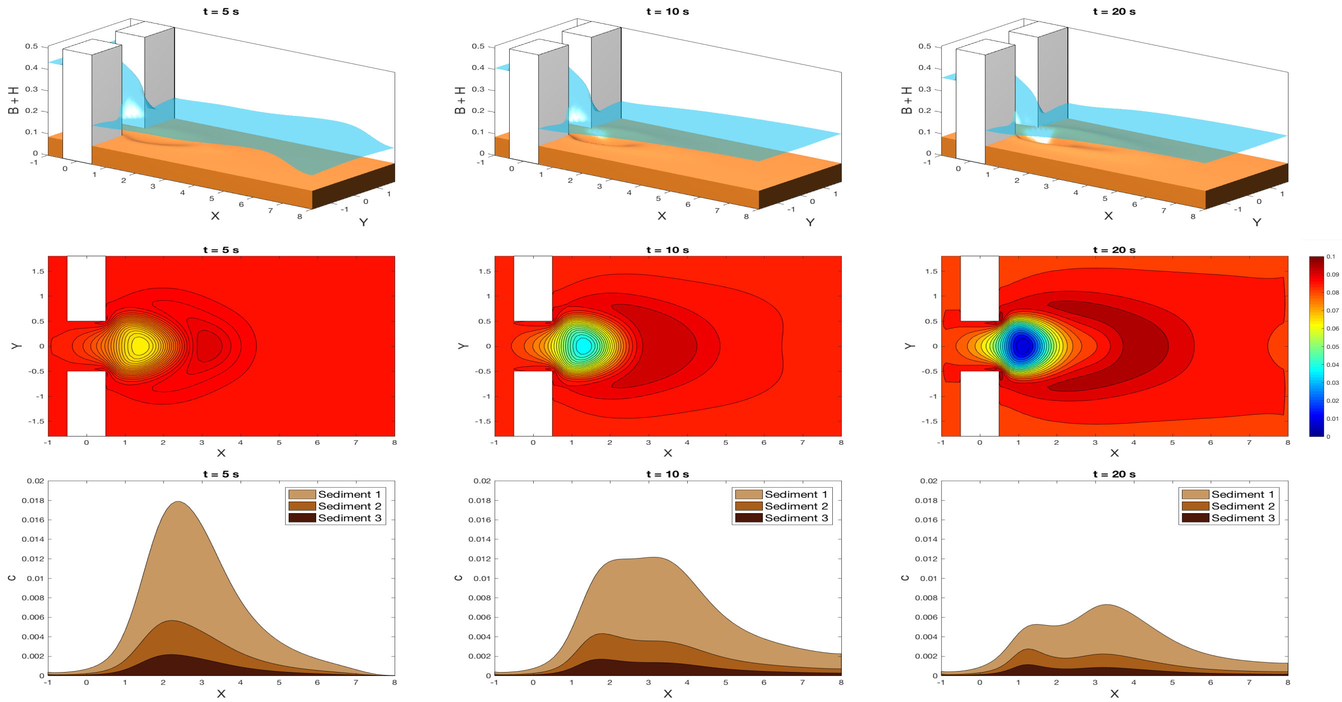

Figure 18: Results obtained for the free-surface (first row), bed-load (second row) and cross-section of the sediment concentration at $y = 0\ m$ (third row) for the dam-break over a three-layer sediment mobile bed at $t = 5\ s$ (first column), $t = 10\ s$ (second column) and $t = 20\ s$ (third column).

with the same initial conditions as in the previous case with the bed formed with a single sediment. The obtained results for the water free-surface, the bed-load and the cross-section of the sediment concentration at $y = 0\ m$ are presented in Figure 18 at $t = 5\ s$, $10\ s$ and $20\ s$. These results are very interesting as more net erosion is obtained due to the small diameter of the sediment fraction than in the simulation using homogeneous beds as in the previous situation. Compared to simulations using the single-layer sediment, more net deposition has also been predicted in this test example. It is also interesting to note that the suspended sediment fractions are very dependent on the sediment mixtures. As the sediment is well distributed and the erosion rates are comparable, we do not observe ripple formation or any other effect of armoring, as the experimental results would demonstrate. The results obtained for this example show that using a detailed description of sediments, it is possible to accurately represent the fractions by the size of sediments constituting the bed. The proposed models perform very well for this example and capture

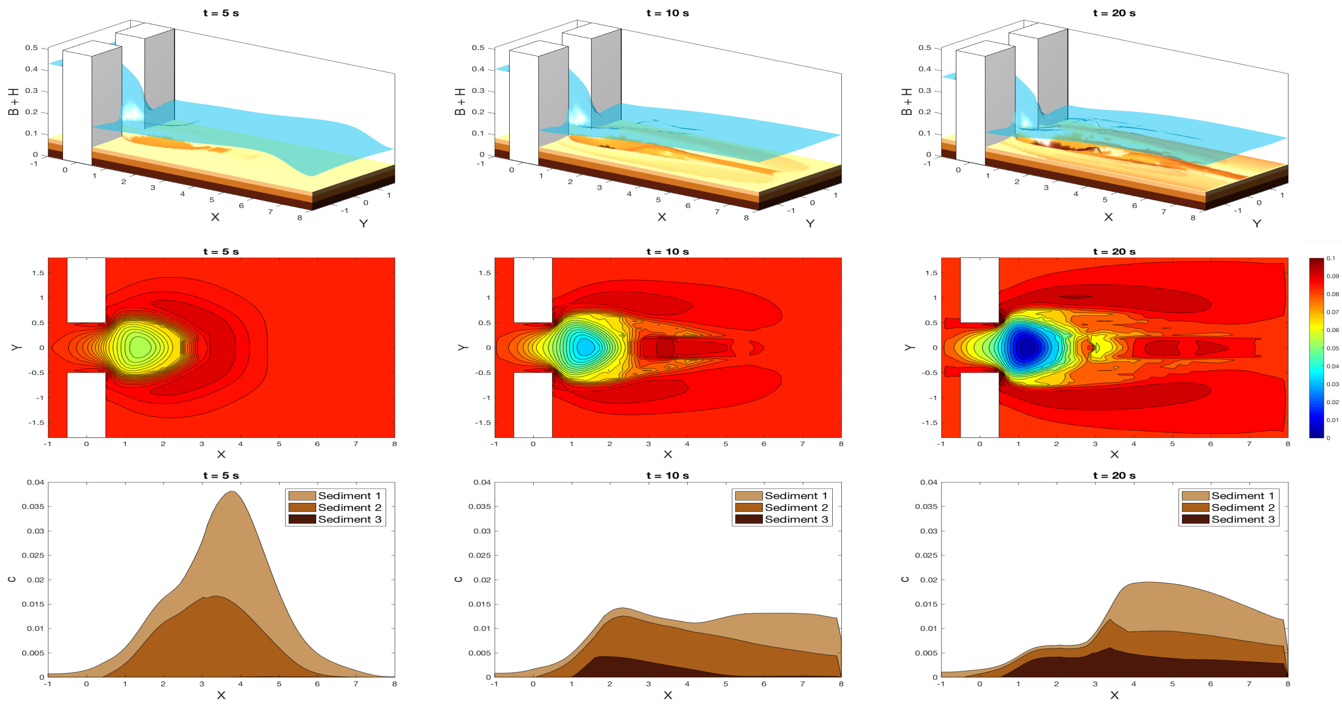

Figure 19: Same as Figure 18 but for the dam-break over a three-layer sediment mobile bed.

the correct flow and sediments structures without requiring complicated techniques or three-dimensional representations for the free-surface flows over heterogeneous beds.

Next, we solve the same problem but using a three-layer bed formed with the sediments as in the previous case. The previous two runs for this test example have shown how a small change in the sediment composition of the bed can cause a large difference in the final bed profile. The objective of this run is to demonstrate the effects of armoring and the creation of ripples, by modifying the bed so that erosion and deposition are no longer uniform and bed variation takes place. This simulation is of interest because it not only has high levels of erosion but also an appreciable level of deposition which makes it difficult in simulations, especially with experimental data. Using the same sediments as in the last simulation, we arrange the initial bed into three layers as

$$B(0,x,y,z) = \begin{cases} \text{Sediment } 1, & \text{if} \quad 0.065\ m \ \leq z < \ 0.085\ m, \\ \text{Sediment } 2, & \text{if} \quad 0.035\ m \ \leq z < \ 0.065\ m, \\ \text{Sediment } 3, & \text{if} \quad 0.0\ m \ \leq z < \ 0.035\ m. \end{cases}$$

The associated parameters for these sediments are summarized in Table 1. The obtained results for water free-surface, bed-load and sediment concentration at three different instants are illustrated in Figure 19. As expected, due to the nonuniform rates of erosion and deposition in the three sediment types and the finely tuned parameters of this simulation, armoring occurs. It is also interesting to note that the total rate of erosion in this case is higher than in the previous simulations. This is because of the high initial rate of erosion in Sediment 1 and the increased near-bed velocity in the flow system from the changing morphology. This simulation shows how, unlike other models tested, the considered model will only induce armoring and ripples with altered bed conditions. These results demonstrate the ability of the FVC method to capture these morphodynamics without generating nonphysical oscillations.

6 Concluding remarks

A class of fast and accurate numerical models has been proposed for the modelling and simulation of two-dimensional shallow water flows over multi-sediment erodible beds. An hyperbolic system of five equations for balance laws with source terms is presented for coupled hydrodynamics, morphodynamics, and suspended sediments. To close the system, a set of empirical formulae for entrainment and deposition terms is considered, along with flux terms for the mass exchange between the multiple layers in sedimentary beds. Although we have used averaged variables in the equations of suspended sediments for the proposed model, each sediment is still handled separately for erosion and deposition. For the numerical solution we consider the finite volume characteristics method, which combines the advantages of the finite volume methods and the method of characteristics. The method consists of a predictor-corrector procedure for which the numerical fluxes are reconstructed in the predictor stage, using the method of characteristics applied to the projected system in the local normal and tangential coordinates. The presented solver satisfies the conservation property and achieves excellent numerical balance between the gradient fluxes and the source terms for the coupled system. No Riemann problem solvers are needed in the proposed method to compute the numerical fluxes. We also consider a consistent vertical discretization of the finite volume type for the multilayer bed to allow for different sediment properties forming the bed. To examine the performance of the proposed models we simulate a wide variety of two-dimensional shallow water flows over multi-sediment movable beds. We have compared numerical results to experimental data and we also performed simulation on single-layer and multilayer sedimentary beds. The results obtained have exhibited accurate predictions of both the hydrodynamics and morphodynamics, with correct conservation properties and stable representations of the water free-surface response to the multilayer erodible beds. Future work will focus on the implementation of these techniques on unstructured meshes accounting for the effects of vegetation, sediment grading, and other morphodynamics features by changing the sediment cell characteristics in the sedimentary bed.

Acknowledgment. The authors would like to thank anonymous referees for giving very helpful comments and suggestions that have greatly improved this paper.

References

[1] K. E. K. Abderrezzak, A. D. Moran, E. Mosselman, J. Bouchard, H. Habersack, and D. Aelbrecht. A physical, movable-bed model for non-uniform sediment transport, fluvial erosion and bank failure in rivers. *Journal of Hydro-environment Research*, 8:95–114, 2013.

[2] F. Benkhaldoun, I. Elmahi, S. Sari, and M. Seaid. An unstructured finite-volume method for coupled models of suspended sediment and bed load transport in shallow-water flows. *International Journal for Numerical Methods in Fluids*, 72:967 – 993, 2013.

[3] F. Benkhaldoun, S. Sari, and M. Seaid. Projection finite volume method for shallow water flows. *Mathematics and Computers in Simulation*, 118:87–101, 2015.

[4] E. Bijker. Some considerations about scales for coastal models with movable bed. *Delft Hydraulics Laboratory*, 50:1–128, 1967.

[5] Hieu Bui, Minh Bui, and Peter Rutschmann. Advanced numerical modeling of sediment transport in gravel-bed rivers. *Water*, 11:550, 03 2019.

[6] V. Caleffi, A. Valiani, and A. Zanni. Finite volume method for simulating extreme flood events in natural channels. *Journal of Hydraulic Resources*, 41:167–77, 2003.

[7] Z. Cao and P. Carling. Mathematical modelling of alluvial rivers: reality and myth. Part I: General overview. *Water Maritime Engineering*, 154:207–220, 2002.

[8] Z. Cao and G. Pender. Numerical modelling of alluvial rivers subject to interactive sediment mining and feeding. *Advances in Water Resources*, 27:533–546, 2004.

[9] Z. Cao, G. Pender, and P. Carling. Shallow water hydrodynamic models for hyperconcentrated sediment-laden floods over erodible bed. *Advances in Water Resources*, 29:546–557, 2006.

[10] Z. Cao, G. Pender, S. Wallis, and P. Carling. Computational dam-break hydraulics over erodible sediment bed. *Journal of Hydraulic Engineering*, 67:149–152, 2004.

[11] S. Chen, C. Yang, and C. Tsou. Bedform development and its effect on bed stabilization and sediment transport based on a flume experiment with non-uniform sediment. *International Journal of Sediment Research*, 2017.

[12] R. Fennema and Chaudhry M. Explicit methods for 2D transient free-surface flows. *J Hydraulic Eng*, 116:1013–34, 1990.

[13] L. Fraccarollo and H. Capart. Riemann wave description of erosional dam-break flows. *Journal of Fluid Mechanics*, 461:183228, 2002.

[14] A. Grass. Sediment transport by waves and currents. *SERC London Cent. Mar. Technol.*, FL29, 1981.

[15] C. Juez, C. Ferrer-Boi, J. Murillo, M. A. Hassan, and Garcìa-Navarro P. A model based on Hirano-Exner equations for two-dimensional transient flows over heterogeneous erodible beds. *Advances in Water Resources*, 87:1 – 18, 2016.

[16] C. Juez, J. Murillio, and P. Garcìa-Navarro. A 2D weakly-coupled and efficient numerical model for transiet shallow flwo and movable bed. *Advances in Water Resources*, 71:03–109, 2014.

[17] G. Karunarathna, D. Reeve, and M. Spivack. Long term morphodynamic evolution of estuaries: An inverse problem. *Estuarine, Coastal and Shelf Science*, 77:385–395, 2008.

[18] G. Kozyrakis. Numerical modeling of sediment transport applied to coastal morphodynamics. *Applied Numerical Mathematics*, 104:30–46, 2016.

[19] A. Kuo and L. Polvani. Nonlinear geostrophic adjustment, cyclone/anticyclone asymmetry, and potential vorticity rearrangement. *Phys. Fluids*, 12:1087–1100, 2000.

[20] X. Liu and A. Beljadid. A coupled numerical model for water flow, sediment transport and bed erosion. *Computers & Fluids*, 154:273–284, 2017.

[21] S. Martìnez-Aranda, J. Murillo, and P. García-Navarro. A 1D numerical model for the simulation of unsteady and highly erosive flows in rivers. *Computers & Fluids*, 181:8 – 34, 2019.

[22] E. Meyer-Peter and R. Müller. Formulas for bed-load transport. *Report on 2nd meeting on international association on hydraulic structures research*, pages 39–64, 1948.

[23] W. Mohtar, A. Junaidi, S. Sharil, and M. Mukhlisin. Representative sediment sizes in predicting the bed-material load for nonuniform sediments. *International Journal of Sediment Research*, 31:79–86, 2016.

[24] N. Morgenstern. Report on Mount Polley tailings storage facility breach, January 2015.

[25] Briganti R., N. Dodd, D. Kelly, and Pokrajac D. An efficient and flexible solver for the simulation of morphodynamics of fast evolving flows on coarse sediments beaches. *International Journal for Numerical Methods in Fluids*, 69:859–877, 2011.

[26] T. Rowan and M. Seaid. Efficient computational models for shallow water flows over multilayer erodible beds. *Engineering Computations*, 37:401–429, 2019.

[27] W. Rubey. Settling velocity of gravel, sand, and silt particles. *American Journal of Science*, 148:325–338, 1933.

[28] G. Simpson and S. Castelltort. Coupled model of surface water flow, sediment transport and morphological evolution. *SIAM J. Numer. Anal.*, 21:1600–1614, 2006.

[29] S. Soares-Franzao. Dam-break flows over mobile beds: Experiments and benchmark tests for numerical models. *Journal of Hydraulic Research*, 50:364–375, 2012.

[30] S. Soares-Frazao and Y. Zech. HLLC scheme with novel wave-speed estimators appropriate for two-dimensional shallow-water flow on erodible bed. *International Journal for Numerical Methods in Fluids*, 66:1019–1036, 2011.

[31] G. Strang. On the construction and the comparison of difference schemes. *SIAM J. Numer. Anal.*, 5:506–517, 1968.

[32] K. Terzaghi, R. Peck, and G. Mersi. *Soil Mechanics in Engineering Practice.* John Wile & Sons Publishers, 1996.

[33] I. Townend. An examination of empirical stability relationships for UK estuaries. *Journal of Coastal Research*, 21:1042–1053, 2005.

[34] L. Van Rijn. Sediment pick up functions. *Journal of Hydraulic Engineering*, 110:1494–1502, 1984.

[35] L. Van Rijn. Unified view of sediment transport by currents and waves. I : Initiation of motion, bed roughness, and bed-load transport. *Journal of Hydraulic Engineering*, 113:649–667, 2007.

[36] K. Vercruysse, R. Grabowski, and Rickson R. Suspended sediment transport dynamics in rivers: Multi-scale drivers of temporal variation. *Earth-Science Reviews*, 166:38–52, 2017.

[37] J. Wang and R. Liu. A comparative study of finite volume methods on unstructured meshes for simulation of 2D shallow water wave problems. *Mathematics and Computers in Simulation*, 53:171–84, 2004.

[38] Z. Wang, R. Fokkink, and A. Langerak. A dynamic-empirical model for estuarine morphology. In *Physics of Estuaries and Coastal Seas*, pages 279–286, Balkema, Rotterdam, 1998.

[39] W. Wu and S. Wang. Formulas for sediment porosity and settling velocity. *Journal of Hydraulic Engineering*, 132:858–862, 2006.

[40] D. Zhao, H. Shen, J. Lai, and G. Tabios. Approximate riemann solvers in fvm for 2D hydraulic shock wave modelling. *Journal of Hydraulic Engineering*, 122, 1996.

[41] J. Zhao, I. Özgen-Xian, D. Liang, T. Wang, and R. Hinkelmann. A depth-averaged non-cohesive sediment transport model with improved discretization of flux and source terms. *Journal of hydrology*, 570:647–665, 2019.